Supplementary information

A dynamically reprogrammable metasurface with self-evolving shape morphing

Table of Contents

Supplementary Note S1: Fabrication procedures for the metasurface

Sacrificial layer

1. Clean silicon wafers with acetone and methanol.

2. Spin coat PMMA to produce a sacrificial layer (3000 rpm, 30 s; bake at 180 °C, 30 s)

Bottom PI layer

3. Spin coat PI2545 (1500 rpm, 30s; bake at 110 °C, 180 s; bake at 150 °C, 180 s; vacuum bake at 260 °C, 45 min; fully cure)

Metal layer

4. Deposit Ti/Au (10 nm/300 nm in thickness) using electron-beam evaporation.

5. Define metal pattern using photoresist (S1813, 3000 rpm) and wet etching (Au/Ti etchant).

Top PI layer

6. Spin coat PI2545 (1500 rpm, 30s; bake at 110 °C, 180 s; bake at 150°C, 180 s; vacuum bake at 260 °C, 45 min)

7. Deposit Cu (50 nm) using electron beam evaporation.

8. Define Cu pattern as hard mask using photoresist (S1813, 3000 rpm) and wet etching (Cu etchant).

9. Dry etch of PI in reactive ion etcher (RIE) with CF_3 and CF_4.

10. Remove the Cu hard mask using wet etching (Cu etchant).

Transfer printing

11. Undercut PMMA sacrificial layer in acetone.

12. Transfer sample from silicon wafer to water soluble tape.

13. Dissolve water soluble tape with warm water to make sample freestanding.

Supplementary Note S2: Finite element analysis (FEA)

S2.1 Deformation actuated by the Lorentz force

FEA was performed to simulate the deformation of the serpentine-shaped mesh structures actuated by Lorentz force. A home-made python script was combined with the commercial software ABAQUS to model the coupling of electrical current, magnetic field and structural deformation, which was not directly available in ABAQUS[S1]. The detailed process was reported in the supplementary note of a previous paper of our group[S2]. In brief, given the port voltages as boundary conditions, the distribution of electric current density was simulated by ABAQUS, transferred to the python script to calculate the distribution of the Lorentz force per unit volume, and then the force was transferred back to ABAQUS to simulate the deformation. The simulation was divided into several loading steps (typically K = 10~20), with a small portion (1/K) of the total voltages added in each step. Refined mesh with feature size smaller than 1/10 of the ribbon width (b_{PI}) ensured the accuracy. The elastic modulus (E) and Poisson's ratio (v) were E_{PI} = 2.5 GPa and v_{PI} = 0.34, respectively for PI, and E_{Au} = 78 GPa and v_{Au} = 0.42, respectively for Au. The electrical resistivity of Au was $\rho_{\mathrm{Au}} = 2.43\times10^{-8}$ m·Ω.

S2.2 Temperature change due to Joule heating

The temperature change due to Joule heating of a single serpentine was simulated by the structure-electricity-heat coupling module of ABAQUS. The geometry was imported from the deformed shape simulated by the process in Supplementary Note S2.1. The Joule heat per unit volume was calculated by ABAQUS according to the simulated electric current density. Convective heat transfer with air was applied to all external surfaces of the structure. Steady-state heat transfer analysis then gave the balanced temperature distribution. The baseline values of parameters were I = 10 mA, $\rho_{\mathrm{Au}} = 2.43\times10^{-8}$ m·Ω, b_{PI} = 100 μm, $b_{\mathrm{Au}}/b_{\mathrm{PI}}$ = 0.95, h_{Au} = 0.3 μm, and the convective heat transfer coefficient with air H_{Air} = 50 W/(m^2·K).

Supplementary Note S3: Analytical model and scaling law for the deformation actuated by Lorentz force

S3.1 Analytical model of a single serpentine structure

Supplementary Fig. 2a shows the 2D precursor of a single serpentine structure of total length *L*, with two fixed ends. It consists of *N* semi-circular rings, connected by *N*-1 straight ribbons with length *H*. The distance between the two adjacent straight ribbons is $\lambda = L/N$ (measured from the central axis, $\lambda << L, H$). The semi-circular rings at the two ends of the serpentine structure are also connected by straight ribbons (length *H*/2) to the bonding sites. The *n*-th semi-circular ring is located at $Y = Y_n = -L/2 + (n-1)\lambda$. The cross-sectional width (b_{PI}) and thickness (h_{PI}) of the semi-circular rings and straight ribbons are uniform, with the Au thickness being much smaller than PI thickness.

The serpentine structure deforms into 3D when it is placed in uniform magnetic field *B* (along negative *X*-direction in Supplementary Fig. 2a) and actuated by electric current *I*. For the level of deformation studied in this manuscript (i.e. maximum out-of-plane displacement *u*/*L* on the order of 10%), the following simplifications can be made. The semi-circular ring undergoes only out-of-plane (*Z*- direction) rigid-body displacement $u_Z\left(Y_n\right)$ with no rotation such that it remains horizontal. The straight ribbon undergoes out-of-plane displacement (denoted by Δ_n for the straight ribbon that connects the semi-circular ring *n* to *n*-1) and bending. The boundary conditions are $\Delta_n\left[\left(-1\right)^{n-1}\frac{L}{2}\right] = u_Z\left(Y_n\right)$, $\Delta_n\left[\left(-1\right)^{n}\frac{L}{2}\right] = u_Z\left(Y_{n-1}\right)$ and $\frac{\mathrm{d}\Delta_n}{\mathrm{d}X}\left(\pm\frac{L}{2}\right) = 0$, and following force balance the internal force in *Z*- direction is $P_n = -BIY_n$. Based on beam theory,

$$u_Z\left(Y_n\right) - u_Z\left(Y_{n-1}\right) = \frac{P_n H^3}{E_{\mathrm{PI}} b_{\mathrm{PI}} h_{\mathrm{PI}}^3} = -\frac{BIH^3}{E_{\mathrm{PI}} b_{\mathrm{PI}} h_{\mathrm{PI}}^3} Y_n, \tag{S1}$$

where $E_{\mathrm{PI}} b_{\mathrm{PI}} h_{\mathrm{PI}}^3$ is the bending rigidity with the contribution of Au layer neglected, as Au thickness (0.3 μm) is much smaller than PI thickness (~10 μm). Considering that $\lambda << L$ and the serpentine structure is fixed at two ends, the maximum out-of-plane displacement is

$$u = u_Z\left(Y = 0\right) = -\frac{BIH^3}{E_{\mathrm{PI}} b_{\mathrm{PI}} h_{\mathrm{PI}}^3}\sum_{n=1}^{N/2} Y_n \approx -\frac{BIH^3}{E_{\mathrm{PI}} b_{\mathrm{PI}} h_{\mathrm{PI}}^3 \lambda}\int_{-L/2}^{0} Y\mathrm{d}Y = \frac{BIH^3 L^2}{8E_{\mathrm{PI}} b_{\mathrm{PI}} h_{\mathrm{PI}}^3 \lambda}. \tag{S2}$$

In Eq. (S2), *BIL* is the effective Lorentz force and $\frac{E_{\mathrm{PI}} b_{\mathrm{PI}} h_{\mathrm{PI}}^3 \lambda}{H^3 L}$ may be defined as the effective rigidity of the serpentine structure, such that the displacement is proportional to the effective force divided by the effective rigidity. This analytical solution (Eq. (S2)) matches well with FEA (see Supplementary Note S2 for details), as shown in Supplementary Fig. 2b. In the FEA validation, the dots are for FEA with the baseline values of parameters being B = 0.15 T, I = 10 mA, H = 2 mm, L = 5 mm, E_{PI} = 2.5 GPa, b_{PI} = 100 μm, h_{PI} = 7.8 μm and λ = 200 μm, and each of these 8 parameters varies independently in its representative range; the straight line corresponds to the analytical solution (Eq. (S2)) with slope being 0.125.

For modest current such that the temperature change due to Joule heating is small and therefore the change in the electrical resistivity (ρ_{Au}) can be neglected, the current I is linearly proportional to the applied voltage V via $I \approx \frac{V \lambda b_{\mathrm{Au}} h_{\mathrm{Au}}}{\rho_{\mathrm{Au}} H L}$ (noticing that λ<<H, L). Therefore, the out-of-plane displacement is related to the voltage via

$$u = \frac{BVH^2 L b_{\mathrm{Au}} h_{\mathrm{Au}}}{8 E_{\mathrm{PI}} b_{\mathrm{PI}} h_{\mathrm{PI}}^3 \rho_{\mathrm{Au}}}. \quad \text{(S3)}$$

S3.2 Scaling law for the deformation of the array of *N* serpentine beams structure

Supplementary Fig. 9 an array of N serpentine beams (along Y-direction, labeled as S_{Y1}, S_{Y2},…, S_{YN}, S_{YN+1},…, S_{Y2N}) connected by N+1 serpentines along X-direction (labeled as S_{X0}, S_{X1},…, S_{XN}). There is no metal layer in serpentine S_{Xi} (i = 0,1,…,N) such that the electric currents in serpentine S_{Yj} and S_{YN+j} are the same (denoted as I_j), and each of I_j can be applied independently via port voltages. Applying voltage V_j to induce electric current I_j in only two serpentines (S_{Yj} and S_{YN+j}), dimensional analysis suggests that the effective Lorentz force is BI_jL and the effective rigidity of the serpentine structure is proportional to $\frac{E_{\mathrm{PI}} b_{\mathrm{PI}} h_{\mathrm{PI}}^3 \lambda}{H^3 L}$, such that the displacement of node j (intersection of serpentine S_{Yj} and S_{YN+j}), proportional to the effective

force divided by the effective rigidity, follows the same scaling as in Eq. (S2) and Eq. (S3), with a revised slope to account for the mechanical coupling among the serpentines, i.e. $u_n \propto \frac{BI_j H^3 L^2}{E_{\mathrm{PI}} b_{\mathrm{PI}} h_{\mathrm{PI}}^3 \lambda}$ and $u_n \propto \frac{BH^2 L b_{\mathrm{Au}} h_{\mathrm{Au}}}{E_{\mathrm{PI}} b_{\mathrm{PI}} h_{\mathrm{PI}}^3 \rho_{\mathrm{Au}}} V_j$. When all the port voltages V_j are applied simultaneously, under the linear assumption such that the principal of linear superposition applies, the displacements u_n are still linearly dependent on port voltages V_j and the coefficients in the linear relationship scale with $\frac{BH^2 L b_{\mathrm{Au}} h_{\mathrm{Au}}}{E_{\mathrm{PI}} b_{\mathrm{PI}} h_{\mathrm{PI}}^3 \rho_{\mathrm{Au}}}$.

S3.3 Scaling law for the deformation of the *N*×*N* structures

Supplementary Fig. 10 shows a serpentine-shaped mesh structure consisting of $N \times (N+1)$ serpentines along *X*- direction (labeled as S_1, S_2,…, $S_{N(N+1)}$, length L_S) connected by $(N+1) \times N$ serpentines along *Y*-direction (labeled as $S_{N(N+1)+1}$, $S_{N(N+1)+2}$,…, $S_{2N(N+1)}$, length L_S). The geometries of all the serpentines are the same. Port voltages V_j (j = 0,1,…,4*N*) are applied at the peripheries of the structure to induce electric currents I_i (i = 1,2,…,2*N*(*N*+1)) in the serpentines. The resistance of each serpentine is $R \approx \frac{\rho_{\mathrm{Au}} L_S H}{\lambda b_{\mathrm{Au}} h_{\mathrm{Au}}}$ (noticing that $\lambda << H, L_S$). Given *N*, L_S is linearly proportional to the overall size *L* of the structure, such that $R \propto \frac{\rho_{\mathrm{Au}} LH}{\lambda b_{\mathrm{Au}} h_{\mathrm{Au}}}$. Therefore, dimensional analysis suggests that the electric currents are linearly dependent on the port voltages via

$$I_i = \frac{\lambda b_{\mathrm{Au}} h_{\mathrm{Au}}}{\rho_{\mathrm{Au}} HL} \sum_{j=1}^{4N} \tilde{D}_{ij} V_j \,, \qquad \text{(S4)}$$

with the dimensionless coefficients $\tilde{D}_{ij}$ depending on the geometry. Dimensional analysis also suggests that the displacements induced by current I_i follows the same scaling as in Eq. (S2) with a revised slope to account for the mechanical coupling among the serpentines, i.e. $u_n \propto \frac{BH^3 L_S^2}{E_{\mathrm{PI}} b_{\mathrm{PI}} h_{\mathrm{PI}}^3 \lambda} I_i \propto \frac{BH^3 L^2}{E_{\mathrm{PI}} b_{\mathrm{PI}} h_{\mathrm{PI}}^3 \lambda} I_i$ (given *N*). Therefore, under the linear assumption, the principal of linear superposition in combination with Eq. (S4),

suggests that the displacements u_n are linearly dependent on the port voltages V_j and the coefficients in the linear relationship scale with $\frac{BH^2Lb_{\mathrm{Au}}h_{\mathrm{Au}}}{E_{\mathrm{PI}}b_{\mathrm{PI}}h_{\mathrm{PI}}^3\rho_{\mathrm{Au}}}$.

Supplementary Note S4: Theoretical model of the temperature change due to Joule heating

For a segment of Au (length δL) encapsulated in PI (temperature *T*; see Supplementary Fig. 2a for the cross-sectional view), the heat generated by Joule heating per unit time (power) is $W_{\mathrm{Generate}}=\frac{I^2\rho_{\mathrm{Au}}\delta L}{b_{\mathrm{Au}}h_{\mathrm{Au}}}$. The convective heat transfer per unit time with air (H_{Air}—convective heat transfer coefficient, T_{Air}—air temperature) is $W_{\mathrm{Loss}}=2b_{\mathrm{PI}}\left(\delta L\right)H_{\mathrm{Air}}\left(T-T_{\mathrm{Air}}\right)$. Energy balance $W_{\mathrm{Generate}}=W_{\mathrm{Loss}}$ leads to

$$\Delta T=T-T_{\mathrm{Air}}=\frac{I^2\rho_{\mathrm{Au}}}{2b_{\mathrm{PI}}b_{\mathrm{Au}}h_{\mathrm{Au}}H_{\mathrm{Air}}}. \qquad \text{(S5)}$$

As before applying the electric current, temperature of the structure is the same as the air temperature, Δ*T* is also the temperature change due to Joule heating. This analytical solution (Eq. (S5)) is quite accurate to predict the temperature change of a single serpentine structure, as shown in Supplementary Fig. 2c. In the FEA validation, the dots are for FEA of the maximum temperature change in the serpentine, with the baseline values of parameters being I = 10 mA, ρ_{Au} = 2.43×10^{-8} m·Ω, b_{PI} = 100 μm, $b_{\mathrm{Au}}/b_{\mathrm{PI}}$=0.95, h_{Au} = 0.3 μm, and H_{Air} = 50 W/(m^2·K), and each of these 6 parameters varies independently in its representative range; the straight line corresponds to the analytical solution (Eq. (S5)) with slope being 0.5.

For the temperature change Δ*T* to be smaller than a threshold $\Delta T_{\mathrm{Upper}}$ (*i.e.,* the upper limit of the temperature that the material can tolerate or allowed in biomedical application), the upper limit of the electric current is

$$I\le I_{\mathrm{Upper}}=\sqrt{\frac{2b_{\mathrm{PI}}b_{\mathrm{Au}}h_{\mathrm{Au}}H_{\mathrm{Air}}\Delta T_{\mathrm{Upper}}}{\rho_{\mathrm{Au}}}}. \qquad \text{(S6)}$$

Eq. (S6), combined with Eq. (S2), gives the upper limit of the deformation of the single serpentine structure as

$$u_{\mathrm{Upper}} \le \frac{BH^3L^2}{8E_{\mathrm{PI}}h_{\mathrm{PI}}^3\lambda}\sqrt{\frac{2b_{\mathrm{Au}}h_{\mathrm{Au}}H_{\mathrm{Air}}\Delta T_{\mathrm{Upper}}}{b_{\mathrm{PI}}\rho_{\mathrm{Au}}}}\,. \tag{S7}$$

Supplementary Note S5: Experimental characterizations of a single serpentine beam in response to electromagnetic actuation

S5.1 Mechanical behaviors under electromagnetic actuation

Supplementary Fig. 3a shows a schematic illustration of the experimental configuration. The static magnetic field is generated by two parallel disks of Neodymium magnets spaced apart by 55 mm, each with a surface magnetic field of ~2640 Gauss. A single-beam sample (H = 1.2 mm, λ = 190 μm, L = 11.0 mm, 62.4 ± 0.2 Ω in resistance) is placed at the center of the magnetic setup. A customized 3D printed magnet mounting stage can adjust the spacing between the magnets, by balancing the working space and uniformity of the magnetic field, 55 mm is chosen as the designed distance. A movable and rotatable sample stage has a fixed height that is the same as the height of the center of the magnets. Supplementary Fig. 3b, c shows the magnetic flux density in *X*-direction (B_X) measured by a gaussmeter (GMHT201, Apex Magnets) across the center (*O*) along *X-axis* and *Y-axis*, B_X is ~0.224 ± 0.016 T in the center (*O*). In the model-driven process, a nonuniformity of the experimental magnetic field is neglected.

Supplementary Fig. 4a shows a serpentine beam carrying a current density $\boldsymbol{J}$ (along *Y*-axis) deforms locally under the electromagnetic force, $\boldsymbol{F}_{\mathrm{EM}} = \boldsymbol{J} \times \boldsymbol{B}$. The serpentine beam ($\lambda$ << H) exhibits a linear, spring-like behavior when deformed out of the sample plane under the electromagnetic actuation (Supplementary Note S2.1). A side camera (Webcams, ELP, 3840×2160-pixel resolution, 30 fps) monitors the out-of-plane deformation, after which the displacement (u) is quantified via ImageJ 1.x pipeline. This measurement method produces a resolution of 0.005 mm and an uncertainty of ±0.015 mm. Supplementary Fig. 4b shows a representative optical side view of an actuated serpentine beam with an out-of-plane deformation (u) and an unloaded irreversible deformation (u'). The measured displacement increases linearly with the actuation

current ***I*** in the elastic regime, within which the electro-magneto-mechanical behavior of the beam agrees with both analytical solution and finite element analysis study (FEA, Supplementary Note S2.1). When the actuation current exceeds 27.5 mA, the measured u deviates from the analytical prediction, and an irreversible deformation (u') is observed subsequently when unloaded (Supplementary Fig. 4c). Based on the experimental observations, the single-beam sample can deform to a maximum of 4.2 ± 0.1 mm (*u*/*L* ~38%) while remaining to be fully reversible, with a corresponding maximum current (***I***) of 27.5 mA ($\boldsymbol{J} < 7 \times 10^8\ \mathrm{A/m^2}$, the cross-section area is $3.9 \times 10^{-11}\ \mathrm{m^2}$).

S5.2 Thermal behaviors under electromagnetic actuation

Thermal imaging of a single-beam sample heated by a temperature-controlled hot plate calibrates the infrared camera (FLIR E60). The calibrated camera measures the equilibrium temperature of the sample under a current ranging from 0 to 40 mA (at room temperature of 25 °C). Supplementary Fig. 4d shows the measured temperatures against corresponding applied currents, which is consistent with the analytical prediction validated by FEA (Supplementary Note S2). The temperature change (ΔT) induced by Joule heating under a current of 27 mA is ~35 °C upon equilibrium (at room temperature of 25 °C).

S5.3 Actuation time under electromagnetic actuation

The single-beam sample is actuated by an applied current *I* (*I* = 10 mA, *u*/*L* ~14%). The actuation process is monitored by a side camera (Canon EOS R, 60 fps). Supplementary Fig. 6 shows the sample going through a vibration state before reaching a steady state; the sample is considered to have reached the steady state when the measured displacement (*u*) is identical to the subsequent frame in the recorded video. The experimental observation shows that a steady state can be reached within 0.067 s (Supplementary Fig. 6).

S5.4 Cycling test under electromagnetic actuation

The single-beam sample undergoes a current-controlled high-cycle test. The sample deforms 1000 cycles at a frequency of 1 Hz with a displacement amplitude u monitored by a side camera for both small deformation (u/L ~14%, I = 10 mA) and large deformation (u/L ~ 28%, I = 20 mA). Supplementary Fig. 7a, b shows that the single-beam sample under the current cycles of ±10 mA exhibits a stable deformation behavior over 1000 cycles with a constant displacement amplitude, u = 1.55 ± 0.02 mm (u/L ~14%). Supplementary Fig. 7c, d shows the results of the cycling test under the current amplitude of ±20 mA. The single-beam sample maintains a stable deformation behavior over the first 500 cycles with a constant displacement amplitude, u = 3.08 ± 0.06 mm (u/L ~28%). Upon the remaining 500 cycles, both the mean value and the standard deviation of the displacement amplitude increase with the cycles, with an average amplitude, u = 3.18 ± 0.18 mm (u/L ~ 29%), for the last 100 cycles. Overall, the single-beam sample deforms with an amplitude, u = 3.10 ± 0.12 mm (u/L ~ 28%) under the cycling current of ±20 mA over 1000 cycles at the frequency of 1 Hz.

Supplementary Note S6: Optimization algorithm of the experiment-driven process

S6.1 Loss function and optimization

In the experiment-driven process, the real-time imaging evaluates the difference between the current sample (u_i) and the target (u_i^*), provides an in-situ nodal displacement error analysis. Changes in the actuation, $\boldsymbol{V} = \{V_j\}$, will update the loss function, $f(\boldsymbol{V}) = \sum_i e_i^2$, defined as the sum of square of the error (normalized by system size as $e_i = (u_i - u_i^*)/L$). Sequential Least Squares Programming (SLSQP), a gradient-descent based algorithm with 3-point method computes the Jacobian matrix to minimize the loss function. For each V_j (V_j is the voltage input for j^{th} port), 3-point method requires two function evaluations to calculate the numerical approximation of the Jacobian matrix. Each iteration requires 2×(N+M) function evaluations for Jacobian calculation and a further 2 function evaluations for the absolute step size calculation

to fit into the constraints for a *N*×*M* sample.

Supplementary Fig. 30 shows three representative descending processes of loss function $f(\boldsymbol{V})$ over 15 iterations for a 4×4 sample morphing into shape I, III, IV (see Supplementary Note S7 and Supplementary Fig. 32). According to the experimental observation, $f(\boldsymbol{V})$ (with an initial value $f(\boldsymbol{V}=\boldsymbol{0})$ in the range of 0.05-0.35) descends by ~99.5% to a steady state in 5-15 iterations. A maximum final loss, $f_0 \leq 0.005 f(\boldsymbol{V}=\boldsymbol{0})$, sets one of the stopping criteria to generate the output and a maximum of 15 iterations sets another bound to stop the optimization process.

S6.2 Limitations in experimental-driven optimization

Experimental noises and constraints pose limitations on the performance of the optimization process. The major limiting factors in the current setup are the discrete actuation voltages, the maximum actuation allowed for reversible deformation, and the measurement uncertainties in 3D imaging (δu = 0.016 mm, Supplementary Note S12). The discrete actuation comes from the 12-bit pulse-width modulation (PWM) drivers followed by the voltage amplifier circuits, which provide actuation voltages in the range of 0-6 V in a discrete step of ~0.0015 V. The mechanical and thermal characterizations (Supplementary Note S5) suggest the maximum allowed current for reversible deformation to be 27 mA. FEA simulation provides a linear relation between the current flow ($\boldsymbol{I}$) in each serpentine beam and portal voltage($\boldsymbol{V}$) as $\boldsymbol{I} = \boldsymbol{C}^{\mathrm{I}}\boldsymbol{V}$. This model prediction of $\boldsymbol{I}$ based on applied $\boldsymbol{V}$ serves as a virtual current monitor to set a hard condition for $\boldsymbol{V}$ ensuring that the current is below 27 mA everywhere in the sample.

Supplementary Fig. 31a shows a simulation result of the impact of the experimental noises and constraints on the optimization. The simulation takes the linear model (Eq. 1) with uncertainties and constraints characterized from the experiment and evaluates the final loss f_0 of a 4×4 sample morphing target shape (Fig. 3b) post 15 iterations. The distribution of f_0 from simulation agrees with the experiments

given 1,000 trials with a mode at 3D imaging noise δu = 0.016 mm, 12-bits PWM, and maximum current I_{max} = 27 mA. Supplementary Fig. 31b shows the impact of the discrete voltage on the optimization process without imaging noise. The final loss can reach 1.96×10^{-5} in the case of 12-bit PWM signal. A 20-bit resolution gives a final loss comparable to the ideal situation with continuous voltage which yields a final loss f_0 ~3.3×10^{-5}. Supplementary Fig. 31a–d shows the distribution of f_0 with decreasing imaging noise (δu). The result indicates that distribution broadens as the uncertainty increases. Around 70% of f_0 reaches a value less than 3×10^{-4} when δu = 0.016 mm, which indicates that the yielding rate of the experiment-driven process with a maximum iteration of 15 is around 70%.

S6.3 Speed of the feedback control and optimization cycle

Supplementary Table 1 listed the detailed, representative time budget of each step during one function evaluation for the experiment-driven optimization of a 4×4 sample. A remote computer takes an average of 0.06 s to send the updated values to the peripheral Raspberry Pi to alter the voltages in 16 PWM channels. The algorithm pauses 0.1 s to wait for the sample to settle to its steady state upon actuation. The 3D imaging process consists of three consecutive steps: taking images of the sample from stereo cameras (0.08 s), detecting locations of the nodes in two images using OpenCV-Python *matchTemplate* function (0.11 s), calculating the 3D-recontructed nodal displacements using OpenCV-Python *reprojectImageTo3D* function (0.00 s). It takes a total of 0.19 s to get one feedback from 3D imaging. The remote computer runs the optimization algorithm (0.00 s). Overall, the time expenditure for each loss function evaluation cycle is ~0.35 s. Based on the experimental observation, a 4×4 sample takes an average of ~2.5 min to morph a shape from a zero-actuation initial state.

Supplementary Note S7: The abstract target curves and surfaces

The target curve in Supplementary Fig. 15c is a segment of arc, with the following expression

$$\mathrm{Z}=\sqrt{r^2-X^2}-\left(r-c\right),\ r=\frac{L^2+4c^2}{8c}. \tag{S8}$$

c=0.1L leads to the particular shape in Supplementary Fig. 15c. The target curve in Supplementary Fig. 15d is a sinusoidal function $Z=-c\sin\left(\frac{2\pi X}{L}\right)$. c=0.15L leads to the particular shape in Supplementary Fig. 15d.

The target shapes in the dynamic process in Fig. 1d, and the shapes studied in Fig. 3 and Supplementary Fig. 32 are defined by the following functions, with Z denoting the out-of-plane coordinate, and X and Y denoting the in-plane coordinates.

Function 1

$$r=\frac{a^2+c^2}{2c}$$
$$Z=\begin{cases}\sqrt{r^2-X^2-Y^2}-\left(r-c\right) & \sqrt{X^2+X^2}\le a\\ 0 & \sqrt{X^2+Y^2}>a\end{cases}. \tag{S9}$$

The ‘growing up’ process is simulated by a=0.5L, and c increasing from 0 to 0.3L. Shape I in Supplementary Fig. 32 is defined by a=0.5L and c=0.2L.

Function 2

$$Z=c\exp\left[-\frac{\left(X-X_{\mathrm{c}}\right)^2+\left(Y-Y_{\mathrm{c}}\right)^2}{a^2}\right]. \tag{S10}$$

The ‘moving around’ process in Fig. 1d is simulated by c=0.2L, a=0.4L, and changing X_{c} and Y_{c} such that the point with the maximum Z- coordinate moves along a path in the XY plane. The prescribed path in Fig. 1d starts at (X_{c}, Y_{c}) = (0, 0), moves to ($0.2\sqrt{2}$ L, 0), moves circularly with $\sqrt{X_{\mathrm{c}}^2+Y_{\mathrm{c}}^2}=0.2\sqrt{2}L$, and then back to (0, 0). Shape II in Supplementary Fig. 32 is defined by X_{c} = Y_{c} = 0.2L, a = 0.4L, and c = 0.2L.

Function 3

$$Z=\sum_{i=1,2}c_i\exp\left\{-\frac{\left[X+\left(-1\right)^i X_{\mathrm{c}}\right]^2+\left[Y+\left(-1\right)^i Y_{\mathrm{c}}\right]^2}{a^2}\right\}. \tag{S11}$$

The first a few shapes of the ‘splitting up’ process in Fig. 1d is simulated by c_1 = c_2 = 0.2L, a = 0.32L, and X_{c}

and Y_c changing from 0 to 0.2L, with the last one denoted by shape A. Each shape is scaled such that the maximum Z coordinate is 0.2L. The last shape of the 'splitting up' process (shape B) is simulated by c_1 = -c_2 = 0.1L, a = 0.4L, and X_c = Y_c = 0.25L. A few shapes are added between shape A and B by interpolating the two shapes to make the process continuous. The 'oscillating' process in Fig. 1d is simulated by X_c = Y_c = 0.25L, a = 0.4L, c_1 = -c_2, and c_1 changing periodically between -0.1L and 0.1L. The target shape in Fig. 3, the same as Shape III in Supplementary Fig. 32, is defined by X_c = Y_c = 0.2L, a = 0.4L, and c_1 = -c_2 = 0.1L.

Function 4

$$Z=\sum_{\substack{i=1,2\\ j=1,2}}(-1)^{i+j}\,c\exp\left\{-\frac{\left[X+(-1)^{i}X_{c}\right]^{2}+\left[Y+(-1)^{j}Y_{c}\right]^{2}}{a^{2}}\right\}. \tag{S12}$$

Shape IV in Supplementary Fig. 32 is defined by X_c = Y_c = 0.25L, a = 0.4L, and c = 0.1L.

Function 5

$$Z=\begin{cases}\dfrac{c}{2}\left[\cos\left(\dfrac{\pi X}{a}\right)+1\right] & |X|\le a\\ 0 & |X|>a\end{cases}. \tag{S13}$$

Shape V in Supplementary Fig. 32 is defined by a = 0.5L and c = 0.2L.

Function 6

$$X'=\frac{\sqrt{2}}{2}X\cos\theta+\frac{\sqrt{2}}{2}Y,\ Y'=-\frac{\sqrt{2}}{2}X+\frac{\sqrt{2}}{2}Y$$

$$Z=\begin{cases}\dfrac{c}{2}\left[\cos\left(\dfrac{\pi X'}{a}\right)+1\right] & |X'|\le a\\ 0 & |X'|>a\end{cases}. \tag{S14}$$

Shape VI in Supplementary Fig. 32 is defined by a = 0.5L and c = 0.1L.

In addition to those shapes presented in the manuscript, the serpentine-shaped mesh structures may also be deformed to form a number of surfaces represented by the general forms of Functions 1~6, as studied in Supplementary Note S10.2.

Supplementary Note S8: Experimental characterization of an array of 8 serpentine beams sample in response to electromagnetic actuation

Supplementary Fig. 15a shows a typical sample (sample length L = 20.6 mm, sample width W = 12.4 mm, vertical serpentine length L_M = 5 mm, horizontal serpentine length L_N = 1 mm) constructed from an array of N (N = 8) serpentine beams. The horizontal serpentines are polyimide (PI) beams and are non-conductive. Consequently, the sample has 8 electrical-controlled and mechanical-coupled serpentine beams. A voltage vector (***V***) of size 16, applied to the peripheral ports (8 pairs of ports), controls the current density (***J***) in each beam. The displacements (u) of the intersections of adjacent serpentine beams (the nodes) define the outline of the deformed shape. For the modal-driven approach, the displacement of the i^{th} node, u_i, is approximately linearly related to the response of the i^{th} node to each j^{th} portal voltage, V_j, as follows:

$$u_i = \sum_{j=1}^{2N} C_{ij} V_j, \text{ for } i = 1, \dots N.$$

The coupling matrix $\boldsymbol{C} = \{C_{ij}\}$ fully describes this approximately linear mechanical system driven by electromagnetic force. Supplementary Fig. 15b shows FEA and experimental characterization of the electro-magneto-mechanical behavior for representative nodes of the array sample provided voltages in the range of 0~2.5 V. A regression analysis on the FEA results (R^2~0.95) provides the coupling coefficients C_{ij} for a linear-system characterization. This linear approximation enables a model-driven approach that optimizes the portal voltages for the precursor array to deform to a mathematically-defined target shape. Supplementary Fig. 15c, d shows the morphing results of the sample targeting spherical and sinusoidal shapes.

Supplementary Note S9: Definition of the error between deformed and target shapes

For the deformed array of N serpentine structures, a continuous 2D curve $Z^{\text{Deform}}(X)$ can be constructed from the nodal positions u_n (n = 0~N+1, u_0 = u_{N+1} = 0) via interpolation. The error between this deformed 2D curve and the target curve $Z(X)$ is then defined as

$$\text{Error}=\frac{1}{L}\sqrt{\frac{1}{L}\int_{-L/2}^{L/2}\left[Z^{\text{Deform}}(X)-Z(X)\right]^2\mathrm{d}X}\,. \tag{S15}$$

Similarly, for the deformed $N \times N$ mesh structure, a continuous 3D surface $Z^{\text{Deform}}(X,\ Y)$ can be constructed from the nodal displacements u_n^m (m = 0~N+1, n = 0~N+1, $u_n^0 = u_n^{N+1} = u_0^m = u_{N+1}^m = 0$) via interpolation. The error between this deformed 3D surface and the target surface $Z(X,\ Y)$ is then defined as

$$\text{Error}=\frac{1}{L}\sqrt{\frac{1}{L^2}\int_{-L/2}^{L/2}\int_{-L/2}^{L/2}\left[Z^{\text{Deform}}(X,\ Y)-Z(X,\ Y)\right]^2\mathrm{d}X\mathrm{d}Y}\,. \tag{S16}$$

Supplementary Note S10: A numerical study on the feasible range of target shapes

To illustrate that the same mesh structure can be deformed to form abundant target shapes, a numerical study is presented in this Supplementary Note on the error (see Supplementary Note 9 for the definition) of the deformed shape for a few classes of target shapes in general form.

S10.1 Target 2D curves

For functions defined in the range $-L/2 \le X \le L/2$ and taking the form $Z=A_1\left[\cos\left(\frac{2\pi X}{L}\right)+1\right]+A_2\left[\cos\left(\frac{4\pi X}{L}\right)-1\right]$, changing the parameters A_1 and A_2 leads to various target 2D curves. The model-driven approach can be applied for the same precursor structure to form many of these 2D curves. The error of the shapes formed by the array of 8 serpentine beams presented in Supplementary Fig.15 is shown in the contour plot of Supplementary Fig. 21a. When the parameters A_1/L and A_2/L are in a wide range, the error is less than 2%, indicating that a number of target curves can be approximated by the deformed structure quite accurately. This error mainly comes from the limitation on the electric current to avoid temperature change from Joule heating (I < 27.5mA), which limits the ability to form target shapes that require large deformation.

The above target curves are symmetric with respect to the vertical axis at X = 0. Similarly, the asymmetric

target 2D curves defined in the range $-L/2 \le X \le L/2$ and taking the form $Z = B_1 \sin\left(\frac{2\pi X}{L}\right) + B_2 \sin\left(\frac{4\pi X}{L}\right)$ can also be formed by the mesh structure quite accurately when B_1/L and B_2/L are in a wide range (Supplementary Fig. 21b).

In a more general case, a target 2D curve $Z(X)$ defined in the range $-L/2 \le X \le L/2$ with $Z(\pm L/2) = 0$ may be expressed by the Fourier series as

$$Z = \sum_{k=1}^{Q} A_k \left[\cos\left(\frac{2k\pi X}{L}\right) + (-1)^{k-1} \right] + \sum_{k=1}^{Q} B_k \sin\left(\frac{2k\pi X}{L}\right). \quad \text{(S17)}$$

The prior study applies to the curves that are symmetric ($B_k = 0$) or asymmetric ($A_k = 0$) with respect to the vertical axis at $X = 0$ and are dominated by the first two terms ($A_{k>2} \approx 0$ and $B_{k>2} \approx 0$). The curves that involve higher order terms may be formed by the structure with more serpentines (i.e. larger N). Supplementary Fig. 22 shows that the array of 16 serpentine beams may form target curves in a wide range with order $Q = 4$ in the Fourier series.

S10.2 Target 3D surfaces

For functions defined in the range $-L/2 \le X,\ Y \le L/2$ and taking the form defined by Function 1 (Eq. (S9)) in Supplementary Note S7, changing the parameters a and c leads to various target 3D surfaces. The model-driven approach can be applied for the same precursor structure to form many of these 3D surface. The error of the shapes formed by the 4 × 4 mesh structure presented in the main text is shown in the contour plot of Supplementary Fig. 23. When the parameters a/L and c/L are in a wide range, the error is less than 2%, indicating that a number of target surfaces can be approximated by the deformed mesh structure quite accurately. Similar analysis is performed to the target 3D surfaces defined by Function 2~6 (Eqs. (S10)–(S14)) in Supplementary Note S7, showing that the same mesh structure can be deformed to various target shapes accurately (Supplementary Figs. 24–28).

Supplementary Note S11: Computational cost for the model-driven approach

S11.1 Linear system

For the $N\times N$ array of serpentine structures presented in the main text, there are $4N$-1 independently controlled port voltages V_1, V_2, …, V_{4N-1} (one port is connected to ground and always has zero voltage). FEA can be performed to establish the relationship between node displacements and port voltages. Applying voltage V_j at port j and keeping the voltages of other ports being zero, FEA predicts the deformation and an approximate linear fitting of the nodal displacements gives $u_i = C_{ij}V_j$. To obtain the coefficient C_{ij} for all voltages, FEA is performed $4N$-1 times, each time for j=1, 2,…, $4N$-1. When all the port voltages are applied simultaneously, the nodal displacements are the superposition of those when the voltage is applied individually due to linearity, i.e. $u_i = \sum_{j=1}^{4N-1} C_{ij}V_j$, such that the nodal displacements can be evaluated rapidly without additional FEA. Therefore, the total number of FEA scales linearly with the system size N, which is acceptable.

S11.2 Nonlinear system

For a nonlinear system, the above linear superposition approach is no longer valid and the nodal displacements are nonlinear functions of the port voltages, i.e. $u_i = G_i\left(V_1, V_2, ...V_{4N-1}\right)$. Taking P values for each voltage, P^{4N-1} times of FEA is needed to obtain the nonlinear function G_i, which is astronomical (e.g. P = 5 and N = 2 lead to $M^{4N-1} \approx 7.8\times10^5$). For the 2×2 array ($N$ = 2) presented in the manuscript, each FEA takes about 1 hour using a workstation (twenty-core, 2.4GHz processor, 64GB memory). This difficulty in the model-driven strategy based on computation is common for nonlinear systems.

Supplementary Note S12: Characterization of the resolution and uncertainty of 3D imaging

Supplementary Fig. 29a is a schematic illustration of the experimental setup for characterization of the resolution and uncertainty of the 3D imaging methods. In the setup, a side camera (Webcams, ELP,

3840×2160-pixel resolution, 30 fps) provides direct imaging of the out-of-plane deformation. Analyzing the images via ImageJ 1.x pipeline gives the ground-truth measurement of the nodal displacement (u_{m}). Two cameras (Webcams, ELP, 3840×2160-pixel resolution, 30 fps) are placed symmetrically side-by-side above the sample to take top-view images. A calibration algorithm (OpenCV-Python *calibrateCamera* function) is applied to a collection of checkerboard images (custom-made, 7×8 squares, 2×2 mm per square) to correct lens distortion[S3]. The sample nodes provide distinctive cross geometry for image registration. A customized template matching algorithm (based on OpenCV-Python *matchTemplate* function) returns nodal central coordinates ($[x_1,\ y_1]$ and $[x_2,\ y_2]$) from the pair imaging in units of pixels (px). A perspective projection matrix[S4] transforms the disparity ($D(x,y)=\sqrt{(x_1-x_2)^2+(y_1-y_2)^2}$) at the estimated location ($[x=(x_1+x_2)/2,\ y=(y_1+y_2)/2]$), to the relative depth between the camera plane and the node, $Z(X,\ Y)$, as,

$$\begin{bmatrix} X \\ Y \\ Z \\ 1 \end{bmatrix} = \begin{bmatrix} 1 & 0 & 0 & 0 \\ 0 & 1 & 0 & 0 \\ 0 & 0 & bf' & 0 \\ 0 & 0 & 0 & 1 \end{bmatrix} \begin{bmatrix} x \\ y \\ 1/D(x,y) \\ 1 \end{bmatrix},$$

where f' is the focal length of the cameras, b is the distance between the two cameras. A transformation algorithm (based on OpenCV-Python *reprojectImageTo3D* function) implements this 2D-to-3D projection and predicts the nodal depth in a unit of pixels (px) as $u_{\mathrm{p}} = Z(X,\ Y)$.

A cycling test on a 4×4 sample (200 actuation cycles of shape IV in Supplementary Fig. 32, 1 Hz) provides a statistical analysis of the 3D-reconstructed depth measurement (u_{p}). From the results, the mean values and standard errors of u_{p} from 200-cycle measurement for the 16 nodes. The distribution of measured depth (u_{p}) at node 1 of the actuated/unactuated state follow a Gaussian distribution with a standard deviation of 0.254/0.246. The result of analyzing the distribution of u_{p} of all 16 nodes reveals that the stereo-imaging method is capable of producing a measurement with a mean standard deviation, δu_p = 0.25 px for all nodes (Supplementary Fig. 29b). The side camera measurement (u_m) has an uncertainty, $\delta u_m \sim \pm 0.015$. Supplementary Fig. 29c shows a linear relation between u_{p} and u_{m} predicted by a Deming regression on

the experimental data as $u_m = au_{\mathrm{p}} + b$, where $a = -0.0664 \pm 2.543 \times 10^{-4}, b = 12.05 \pm 0.038$ (R^2 = 0.997). The regression model defines the 3D-reconstructed nodal displacement, $u(u_{\mathrm{p}}) = u_m(u_p)$. The nodal displacement (u) measured by 3D imaging method has a resolution of ~0.006 mm and an uncertainty of ±0.055 mm.

The pixel form measurement of the *X*-*Y* coordinates can be converted to physical values given a reference scale bar. Renka-Cline gridding matrix method produces an interpolated 3D surfaces from the reconstructed nodal displacement $u(X, Y)$ at three inserted query points between the two nearest nodes.

Supplementary Note S13: Self-evolving of a nonlinear system

A 2×2 sample (*L*/*W* = 25.0 mm, $L_{N/M}$ = 10.0 mm), consisting of serpentine beams without any straight segments connecting the semi-circle parts, represents a metasurface that exhibits an amplified non-linear mechanical behavior in response to the voltage inputs. Supplementary Fig. 36 a–d shows the side-view images of the sample deforming out-of-plane given an increasing voltage to port 1 (Fig. 4d). Centered in the same magnetic setup, with the increase of the voltage input, the out-of-plane bending initially dominates the structure deformation but saturates at a small displacement due to reduced arc length, such that the serpentine beams need to overcome the tensile rigidity much larger than the bending rigidity for further deformation. The goodness of fit (R^2) of a linear regression on this response (for model-driven approach) is 0.8. In the experiment-driven approach, the optimization takes a loss function and stopping criteria of the same form as the 4×4 sample. The experimental observation shows occasional trapping of $f(\boldsymbol{V})$ in local minima. A repeated optimization process overcomes the local-minimum problem in the nonlinear system.

Supplementary Note S14: Self-evolving toward multifunction

Supplementary Fig. 39a shows the illustration of a 3×3 sample (*L*/*W* = 14.8 mm, $L_{N/M}$ = 2.0 mm) with 9 reflective gold patches (Au, 2 mm × 2 mm in size, 300 nm in thickness). The receiving screen (white printer

paper sheets, 55 mm × 80 mm) is placed 40 mm above the sample in parallel to the *XY*-plane. A red laser beam (~650 nm in wavelength and ~1 mm in beam diameter) and a green laser beam (~520 nm in wavelength and ~1 mm in beam diameter) hit on the center of one patch and got reflected. A top camera (Webcams, ELP, 3840×2160-pixel resolution, 30 fps) monitors the reflected laser spots on the receiving screen. The target optical function is to overlap two laser spots on the receiving screen. A customized imaging analysis method detects the centroid coordinates of the red/green laser spots as the current locations on the screen ($[x^{r/g}, y^{r/g}]$, Supplementary Fig. 38a). The target structural function is to keep central nodal displacement (u_5) at -0.5 mm (u_5^* = -0.5 mm). A linear model (provided by FEA) for the sample monitors u_5 given the prescribed actuation. A post analysis via ex-situ 3D imaging shows an agreement between the model prediction and the experimental results.

A loss function $f_{\text{multi}}(\boldsymbol{V})$ (Supplementary Fig. 38b), tailored for the target multifunctionality, is a linear combination of two parts: 1) $f_{\text{opt}}(\boldsymbol{V})$ evaluating the distance between two reflected spots, and 2) $f_{\text{struct}}(\boldsymbol{V})$ evaluating the central nodal error, both normalized to have an initial value of 1 following:

$$f_{\text{multi}}(\boldsymbol{V}) = af_{\text{opt}}(\boldsymbol{V}) + bf_{\text{struct}}(\boldsymbol{V}),$$

$$f_{\text{opt}}(\boldsymbol{V}) = \frac{(x^r - x^g)^2 + (y^r - y^g)^2}{\left(x_0^r - x_0^g\right)^2 + \left(y_0^r - y_0^g\right)^2},$$

$$f_{\text{struct}}(\boldsymbol{V}) = \left(\frac{u_5 - u_5^*}{u_5^*}\right)^2,$$

where $[x_0^{r/g}, y_0^{r/g}]$ is the initial position of red/green spots on the screen. The two target functions are equally weighted with $a = b = 0.5$. The optimization takes the same stopping criteria as the 4×4 sample.

References

[S1] G. Mao et al., Soft electromagnetic actuators. Sci. Adv. **6**, eabc0251 (2020).

[S2] Supplementary Note in: F. Zhang et al., Rapidly deployable and morphable 3D mesostructures with applications in multi-modal biomedical devices. Proc. Natl. Acad. Sci. U.S.A. **118**, e2026414118 (2021).

[S3] Z. Zhang., A flexible new technique for camera calibration. IEEE Transactions on Pattern Analysis and Machine Intelligence, vol. 22, no. 11, pp. 1330-1334, Nov. 2000.

[S4] Haralick, R. M., Solving camera parameters from the perspective projection of a parameterized curve. Pattern Recognition, **17(6)**, 637–645. (1984).

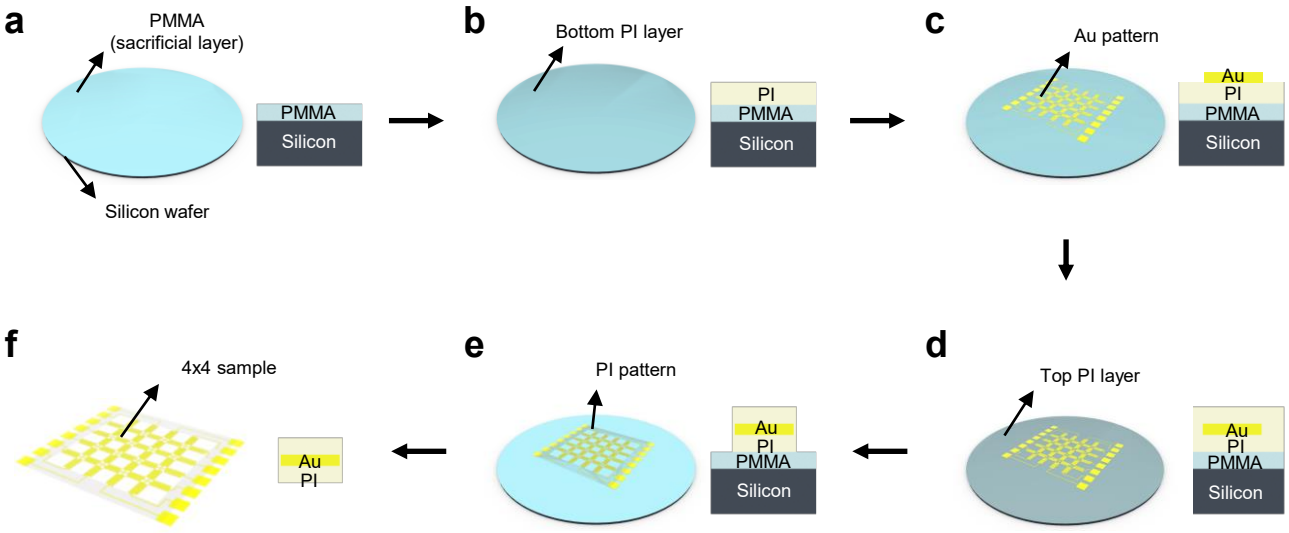

Supplementary Figure 1 | Schematic illustration of the fabrication process. a, Prepare a sacrificial layer (PMMA) on a silicon wafer. **b**, Spin coat a bottom polyimide (PI) layer. **c**, Define the gold (Au) pattern. **d**, Spin coat the top PI layer. **e**, Define the PI pattern. **f**, Undercut sacrificial layer to release the sample from the silicon wafer.

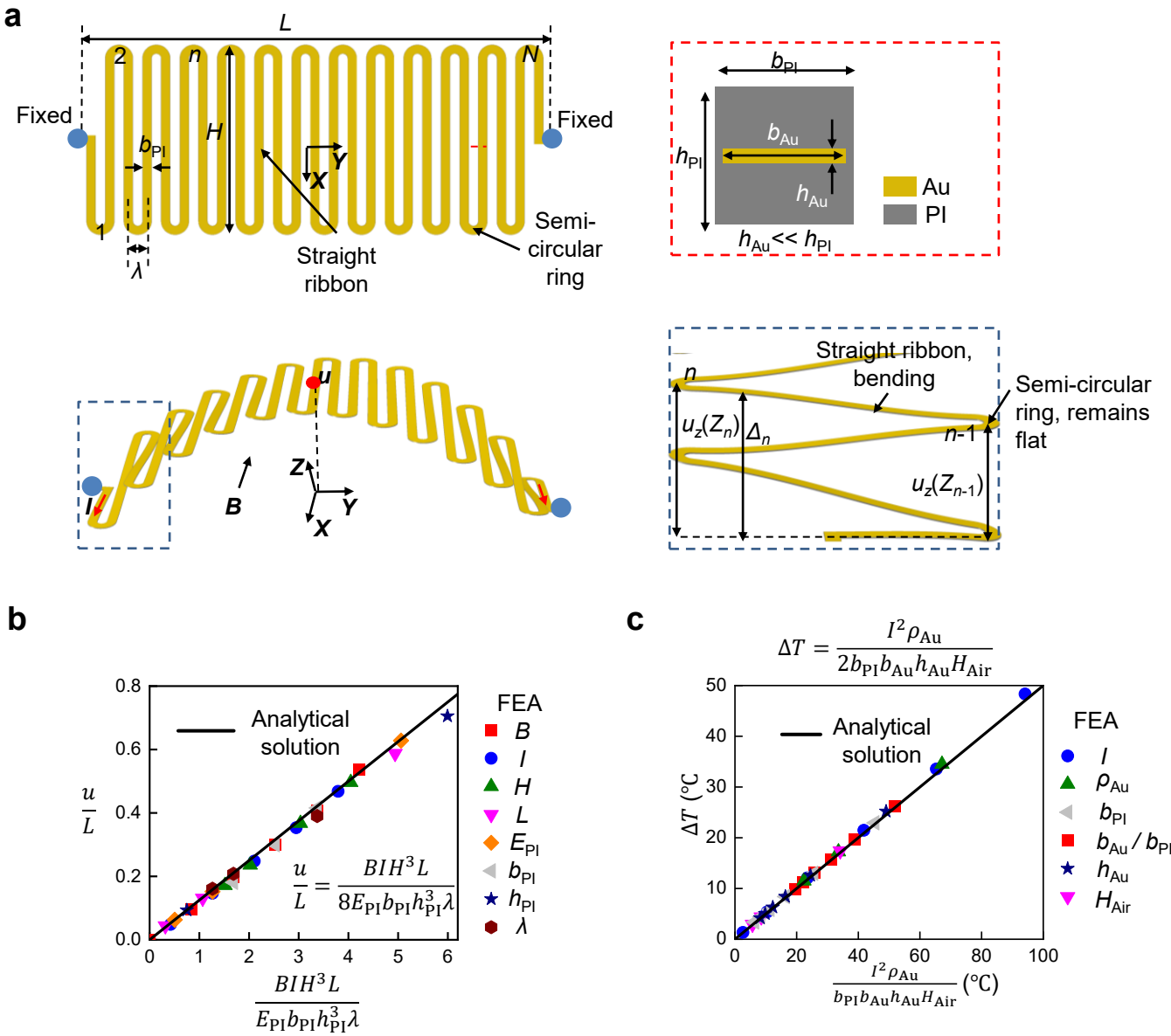

Supplementary Figure 2 | An analytical model and FEA study of the mechanical and thermal behaviors of a single serpentine beam in response to electromagnetic actuation. a, Schematic illustration (top and cross-sectional views) of the initial state (top) and actuation state (bottom) of a serpentine beam **b**, Analytical model and FEA study of the relationship of the maximum out-of-plane displacement *u* vs. the combination of electric current *I*, magnetic field *B*, material and geometry parameters. **c,** An analytical model of the temperature change due to Joule heating, compared with FEA study of the temperature change of the single serpentine beam.

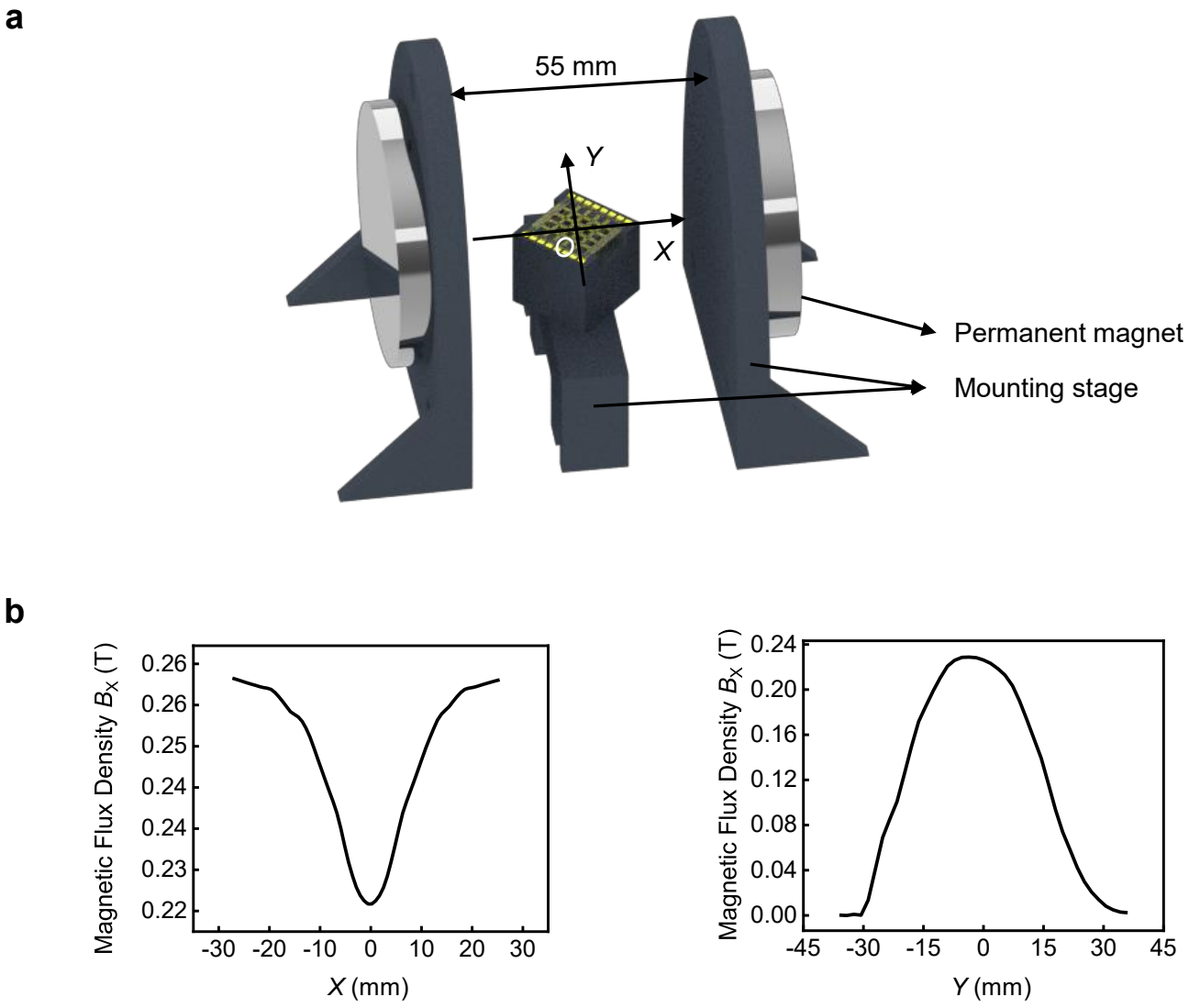

Supplementary Figure 3 | Magnetic setup for Lorentz force actuation. a, Schematic illustration of the magnetic setup consisting of two parallel disks of Neodymium magnets (surface field ~2640 Gauss) fixed on a 3D-printed mounting stage and spaced 55 mm apart. The setup generates a relatively uniform magnetic field of ~0.224 ± 0.016 T in the center (*O*) and perpendicular to the disk plane (*X*-direction). **b**, The magnetic flux density in *X*-direction (B_X) measured by a gaussmeter (GMHT201, Apex Magnets) across the center (*O*) along *X-axis* and *Y-axis*. The model-driven process considers the magnetic field to be uniform with B = 0.224 T and neglects the spatial variation.

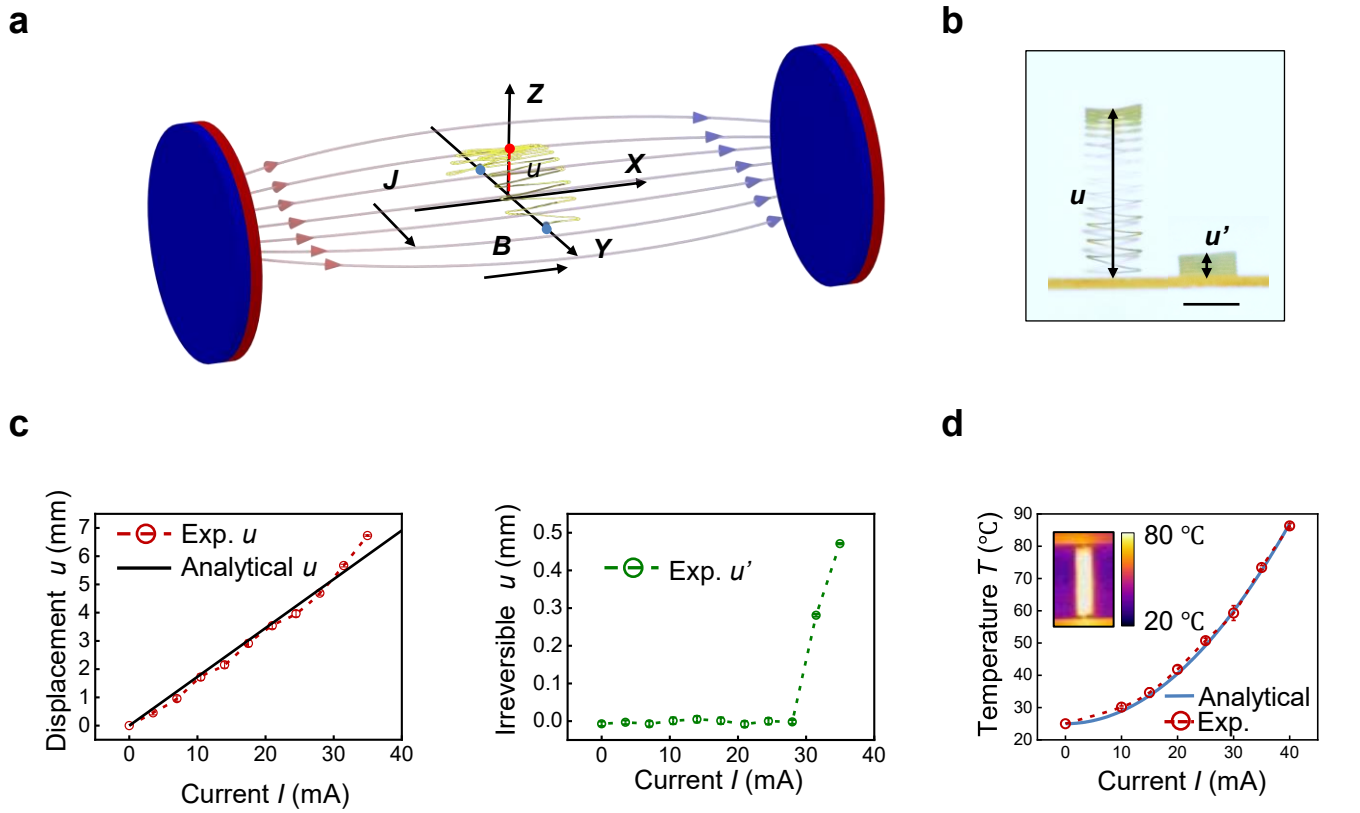

Supplementary Figure 4 | Experimental characterizations of the mechanical and thermal behaviors of a single serpentine beam in response to electromagnetic actuation. a, Schematic illustration of a single beam, placed in a magnetic field ***B*** and carrying a current density ***J***, deforms out-of-plane by a maximum displacement *u*, under an electromagnetic force $\boldsymbol{F}_{\mathrm{EM}} = \boldsymbol{J} \times \boldsymbol{B}$. **b**, Optical images of a representative serpentine beam (side view) deformed to the maximum displacement *u*. If exceeding the elastic limit, an irreversible deformation *u*' will retain after unloading. Scale bar, 1 mm. **c, d, e,** Experimental characterizations of mechanical (c) and thermal (d) behaviors of a single beam under current-controlled electromagnetic actuation in comparison with theoretical predictions.

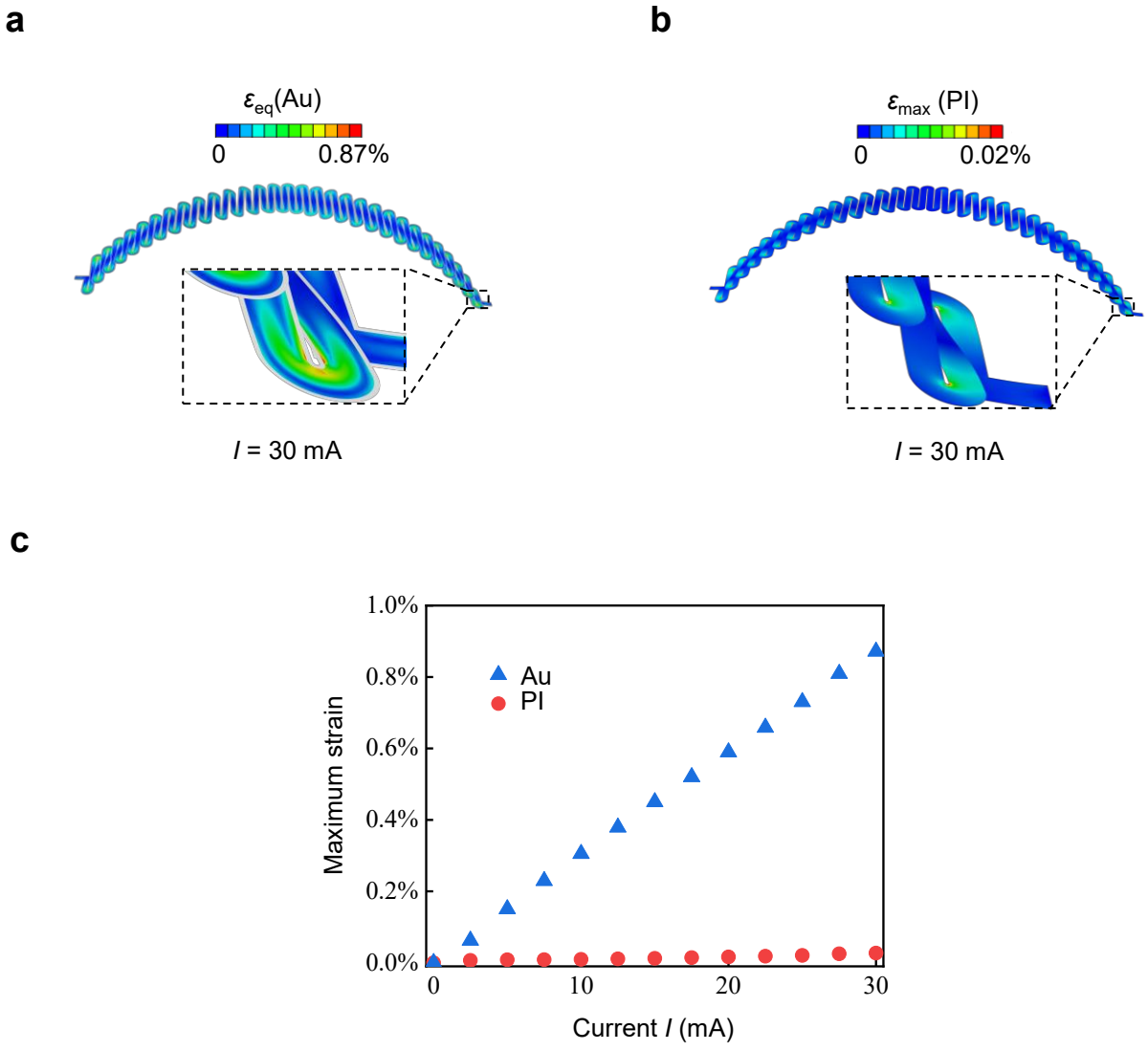

Supplementary Figure 5 | FEA strain study on the deformed single serpentine beam. a, b, Distribution of the equivalent strain in Au (a) and the maximum principal strain in PI (b) when applied current *I* = 30 mA. **c**, The relationship of the maximum equivalent strain in Au and the maximum principal strain in PI vs. applied current *I*.

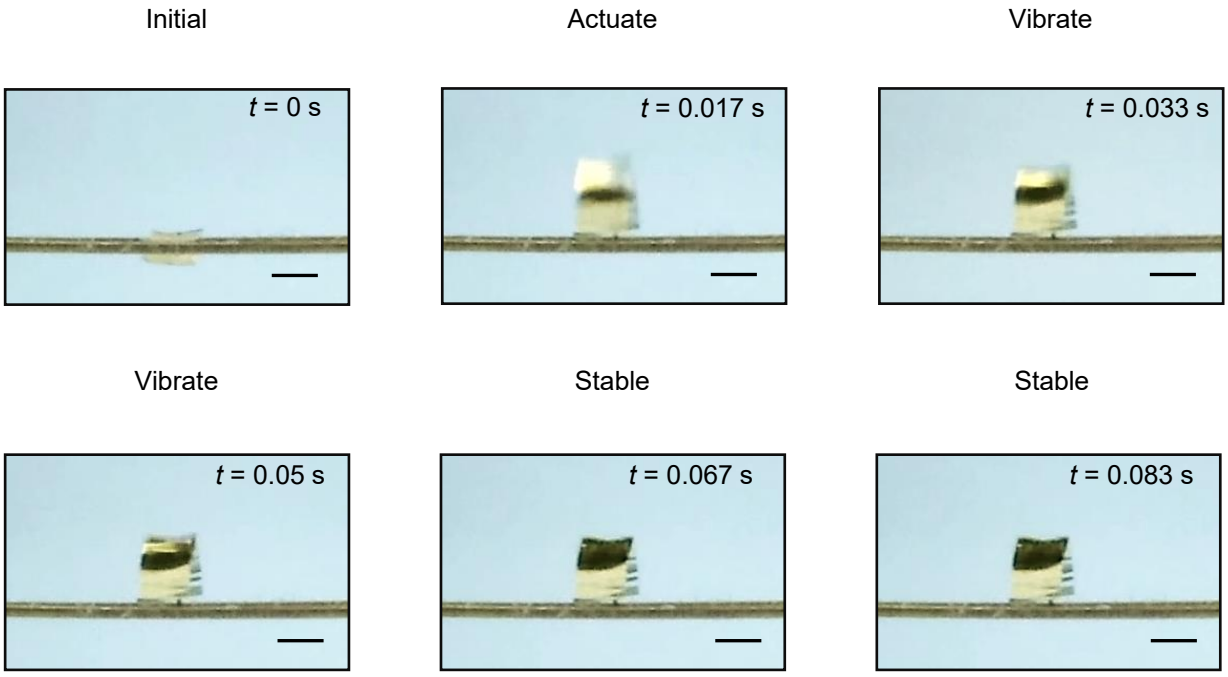

Supplementary Figure 6 | Characterization of the response time of a single-beam sample. A single beam settles to steady state within ~0.07 s upon a step current actuation (applied current *I* = 10 mA). The dynamic process is monitored by a side camera (Canon EOS R, 60 fps). Scale bars, 1 mm.

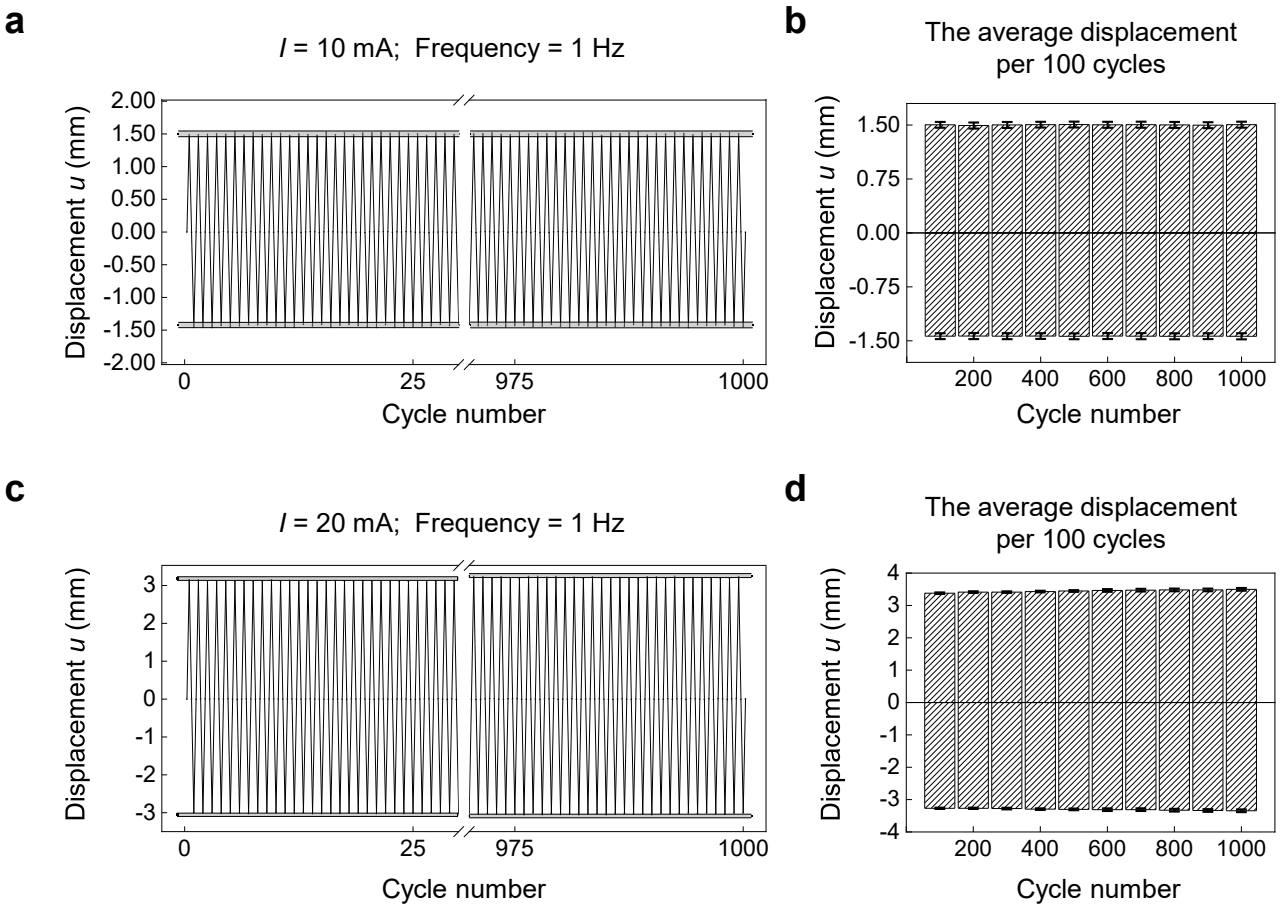

Supplementary Figure 7 | Cyclic mechanical behavior of a single-beam sample. The displacement of the beam is monitored by a side camera during 1000 actuation cycles at 1 Hz with current amplitude of ±10 mA ((a), (b)) and ±20 mA ((c), (d)). Under large deformation (±20 mA) the strain amplitude increases 1% post 1,000 cycles.

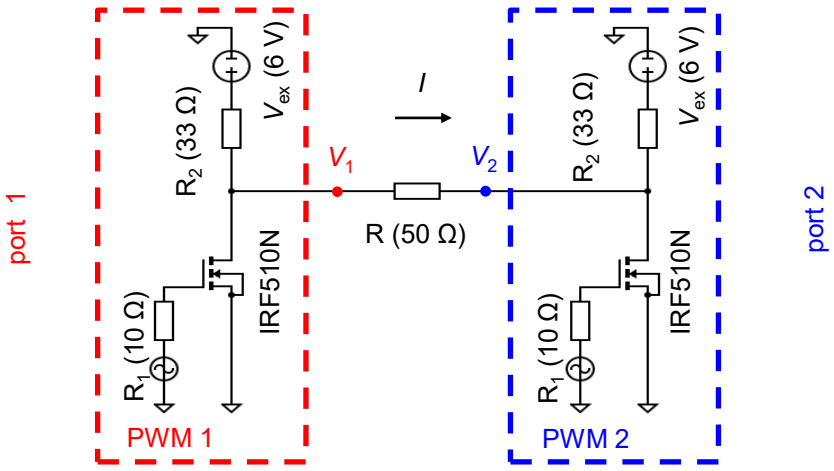

Supplementary Figure 8 | Control and amplification circuits. A resistor of 50 Ω represents the impedance of the sample between the two ports. Each PWM output signal is amplified by a MOSFET (Infineon Tech, IRF510N) using an external power supply (V_{ex} = 6 V).

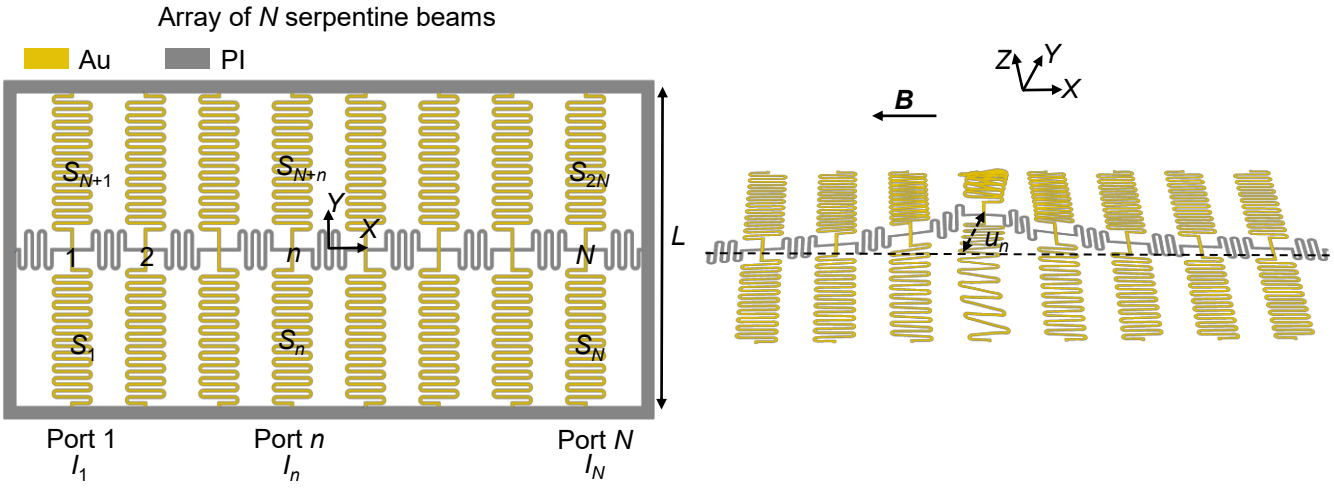

Supplementary Figure 9 | Schematic illustration of an array of *N* serpentine beams.

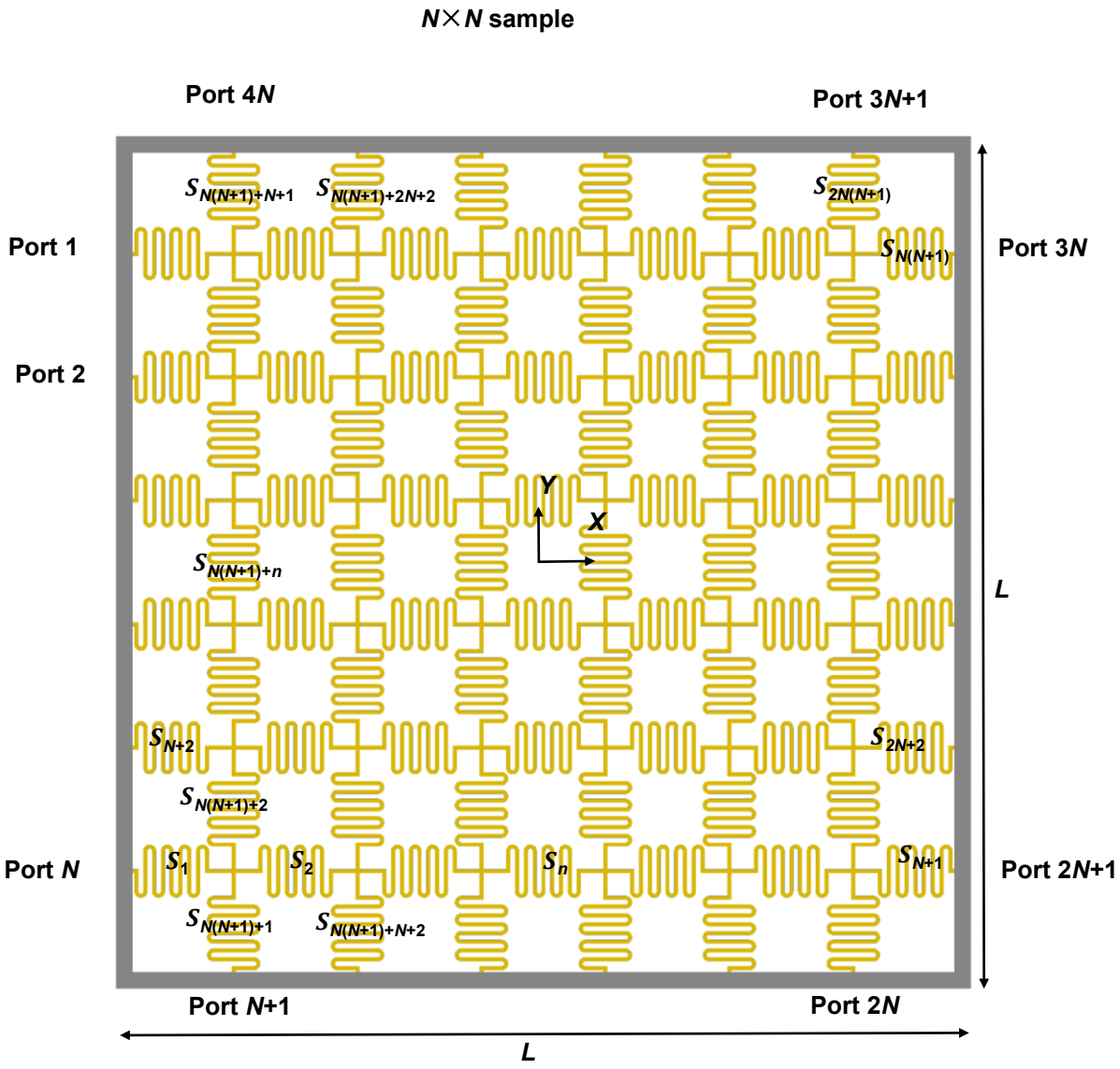

Supplementary Figure 10 | Schematic illustration of an *N*×*N* structures.

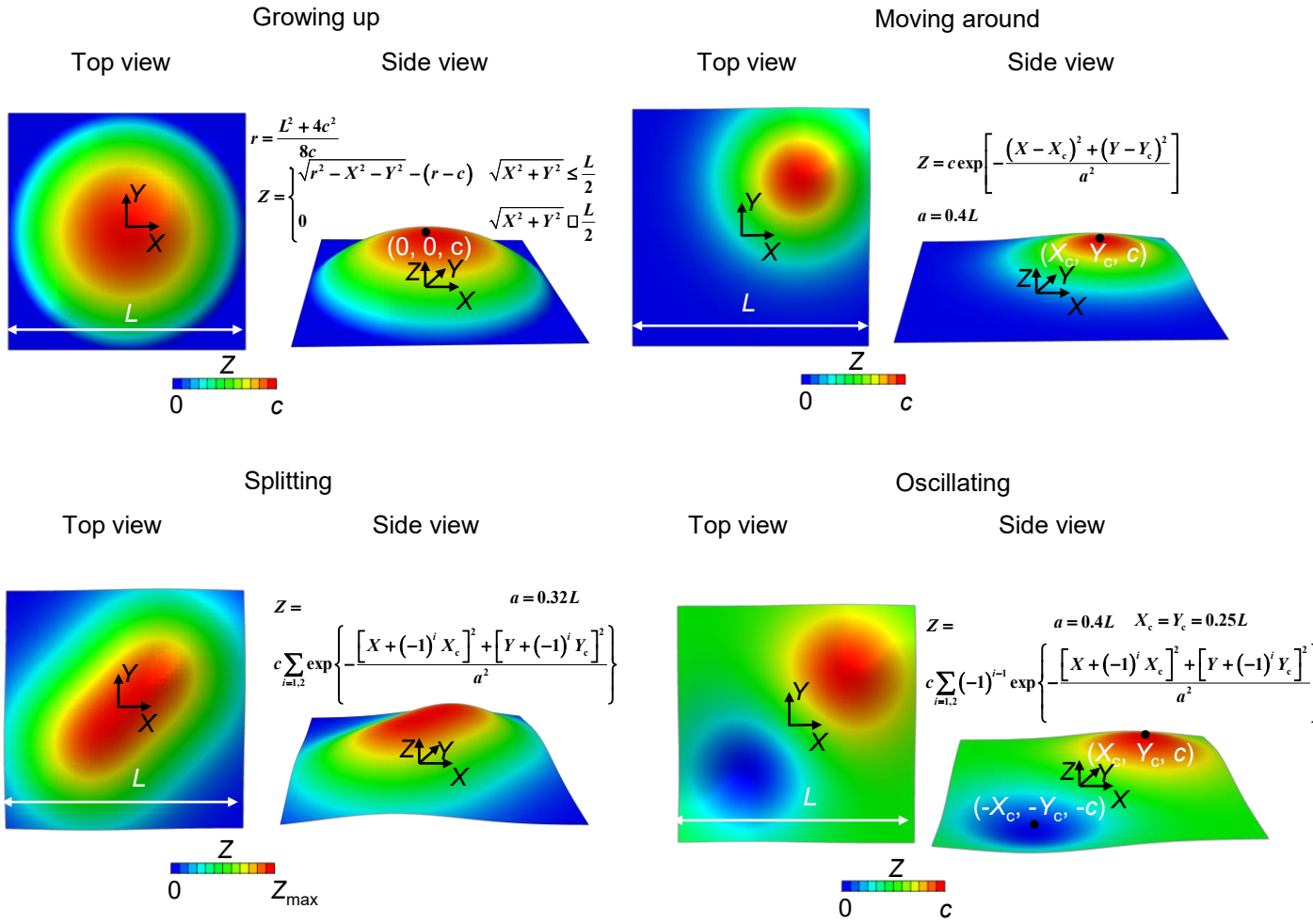

Supplementary Figure 11 | Schematic illustration and formula of 4 implicit shape shifting processes.

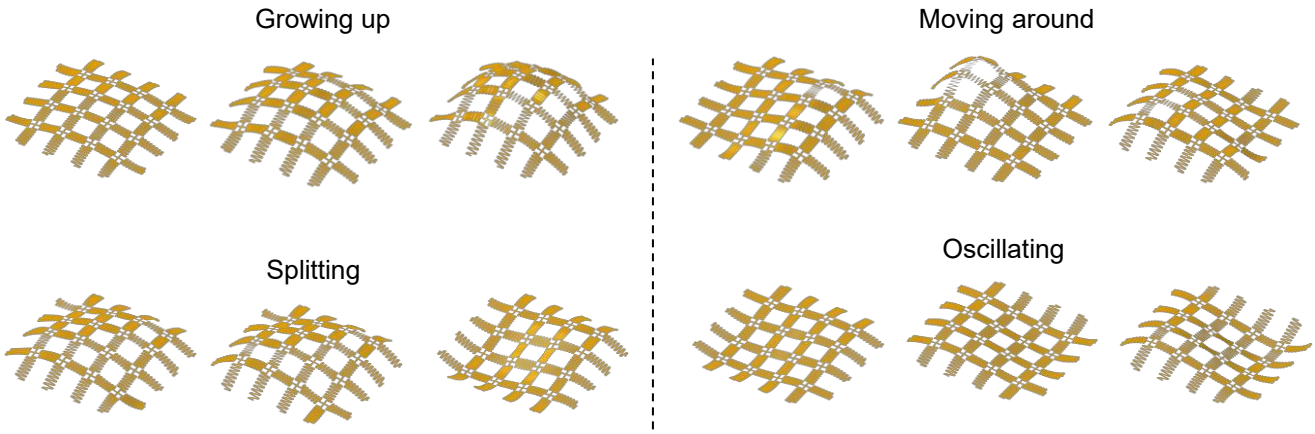

Supplementary Figure 12 | FEA of the 4×4 sample in Fig. 1d

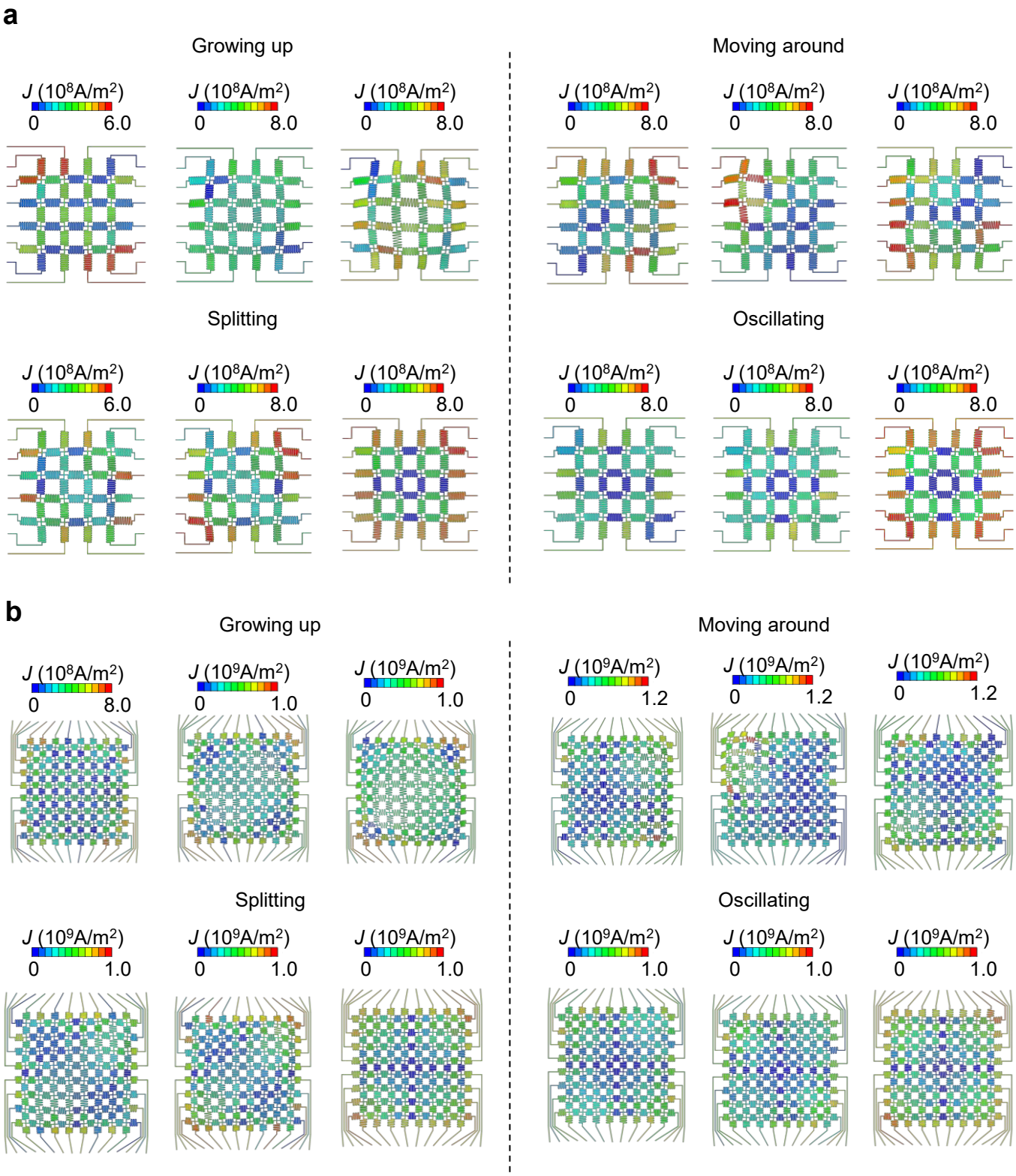

Supplementary Figure 13 | Distribution of current density for the implicit shapes presented in Fig. 1d. a, 4×4 sample. **b,** 8×8 sample.

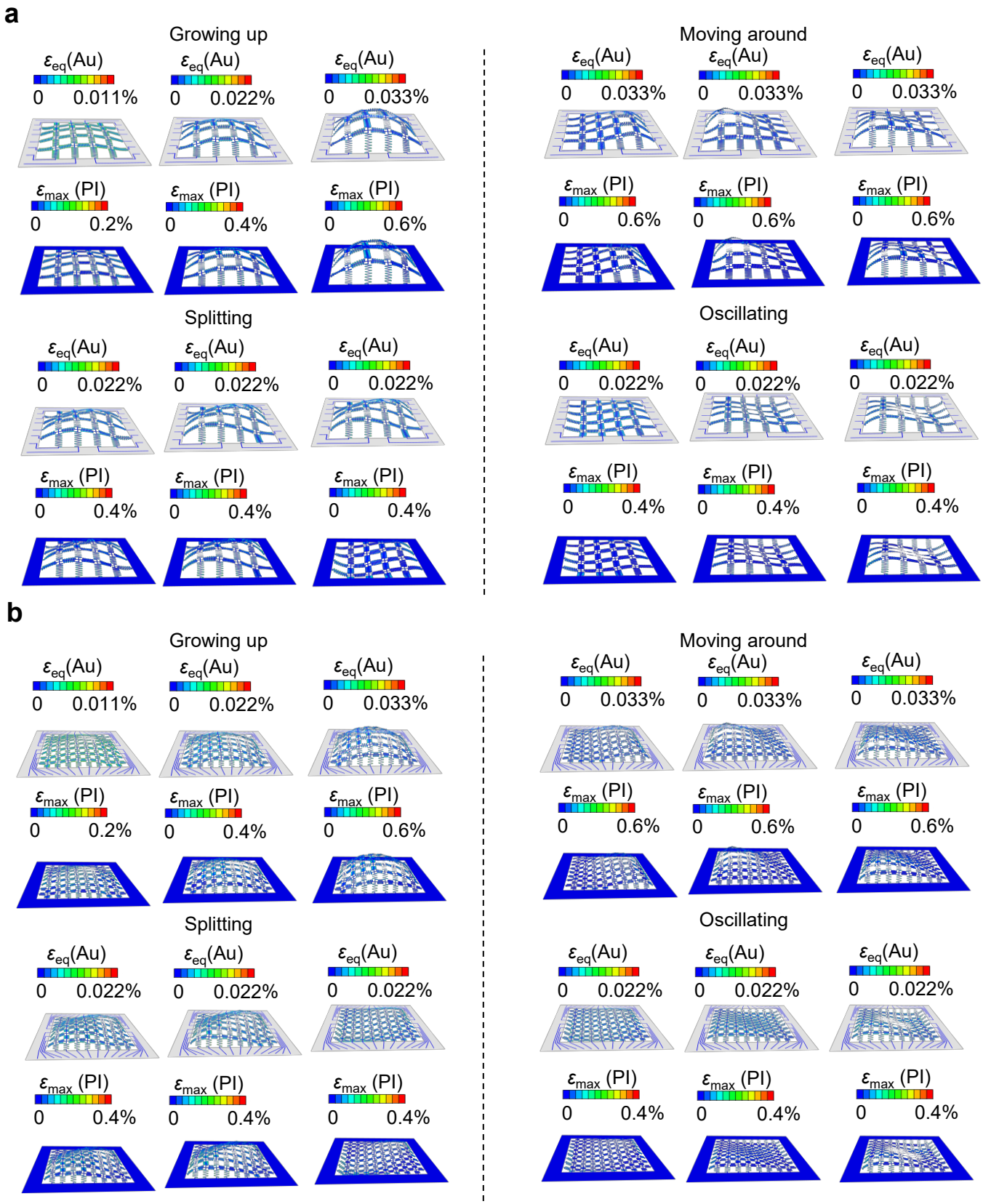

Supplementary Figure 14 | Distribution of the equivalent strain in Au and the maximum principal strain in PI for the implicit shapes presented in Fig. 1d a, 4×4 sample. **b,** 8×8 sample.

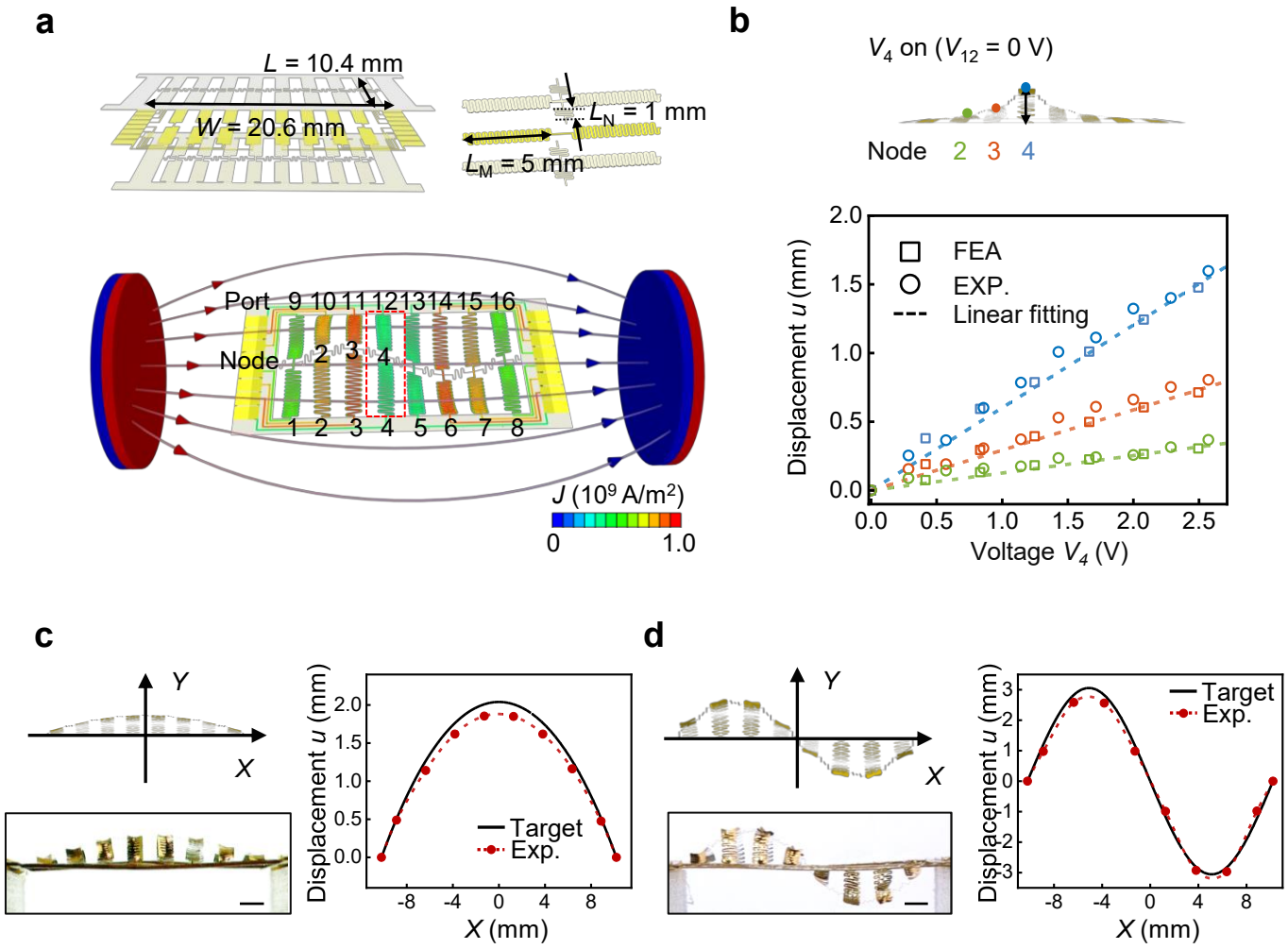

Supplementary Figure 15 | Modeling and experimental investigations of an array of 8 serpentine beams. a, Schematic illustration of an array of 8 serpentine beams with detailed geometries (L = 10.4 mm, W = 20.6 mm, L_N = 5 mm, L_M = 1 mm) specified in the exploded views of the sample and a single serpentine unit. **b,** FEA and experimental investigations confirm an approximately linear relationship between representative nodal displacements and portal voltages for the array sample. **c, d,** FEA and experimental results of the array sample (side view) morphing into a spherical shape (c) and sinusoidal shape (d). See Supplementary Note S6 for the target shape functions. Scale bars, 2 mm.

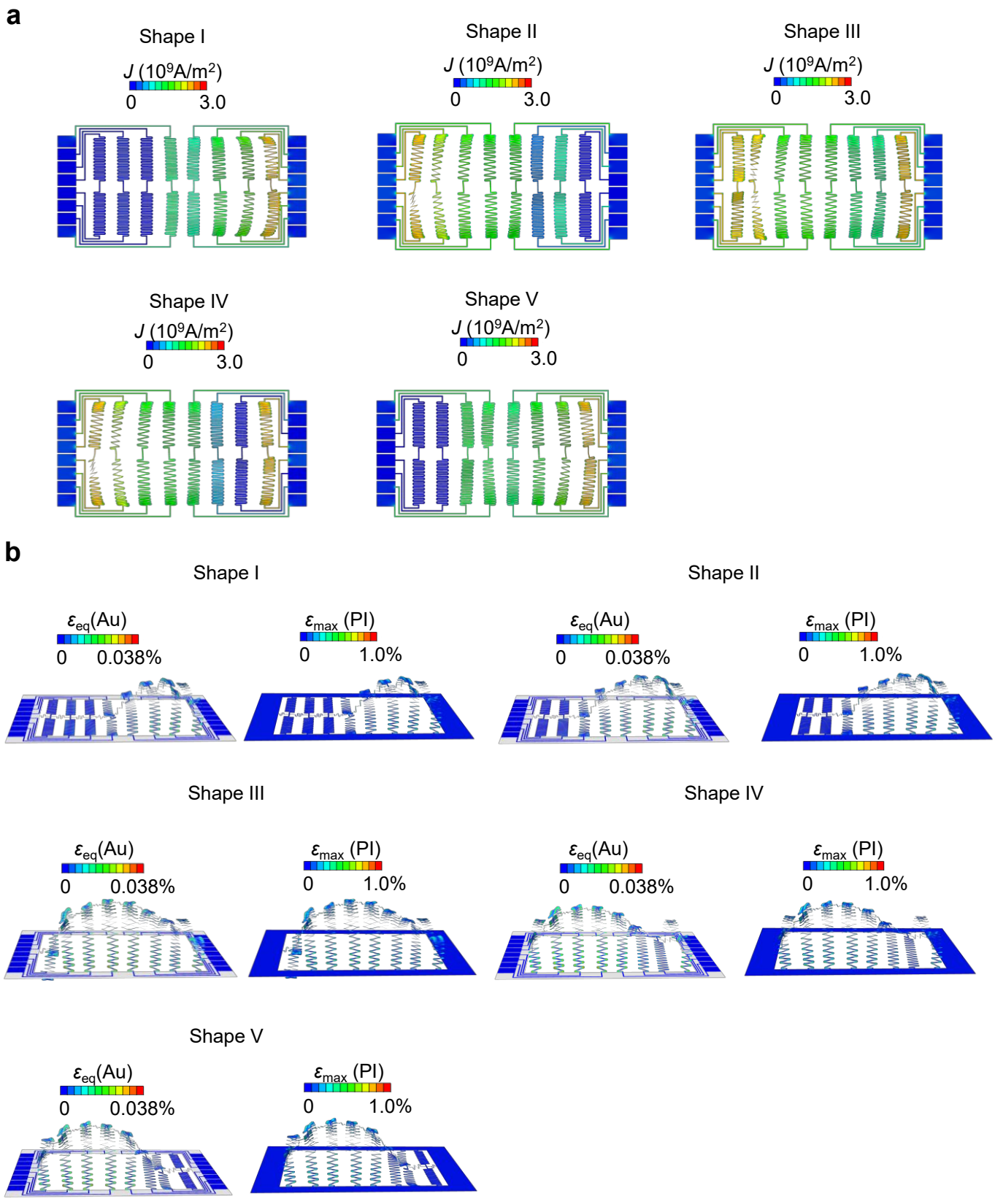

Supplementary Figure 16 | a, b, Distribution of the current (a), and the equivalent strain in Au and the maximum principal strain in PI (b) for the 5 shapes of the dynamic process presented in Fig. 2a.

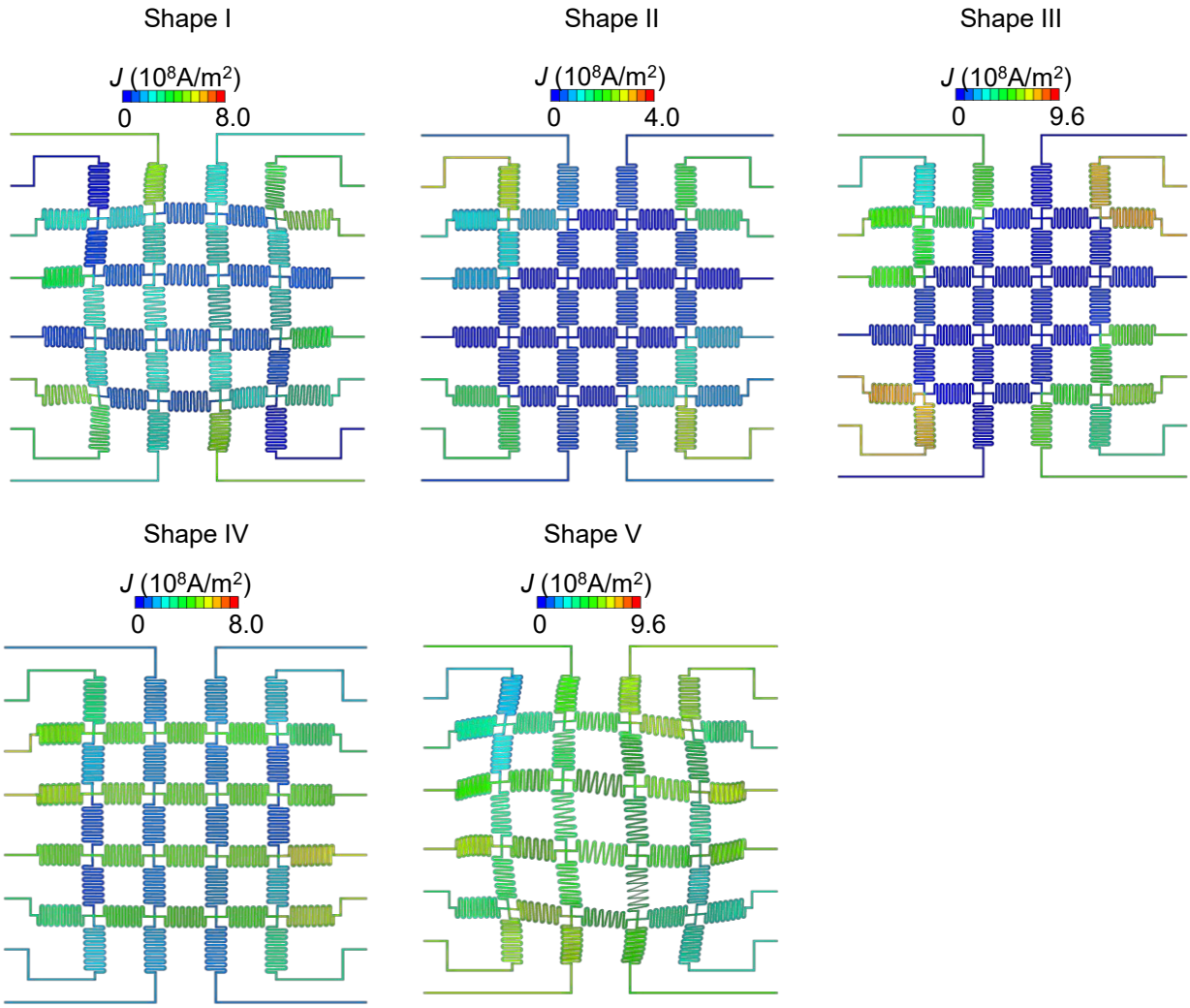

Supplementary Figure 17 | Distribution of current density for the 5 shapes of the falling droplet imitated by the 4x4 sample in Fig. 2b.

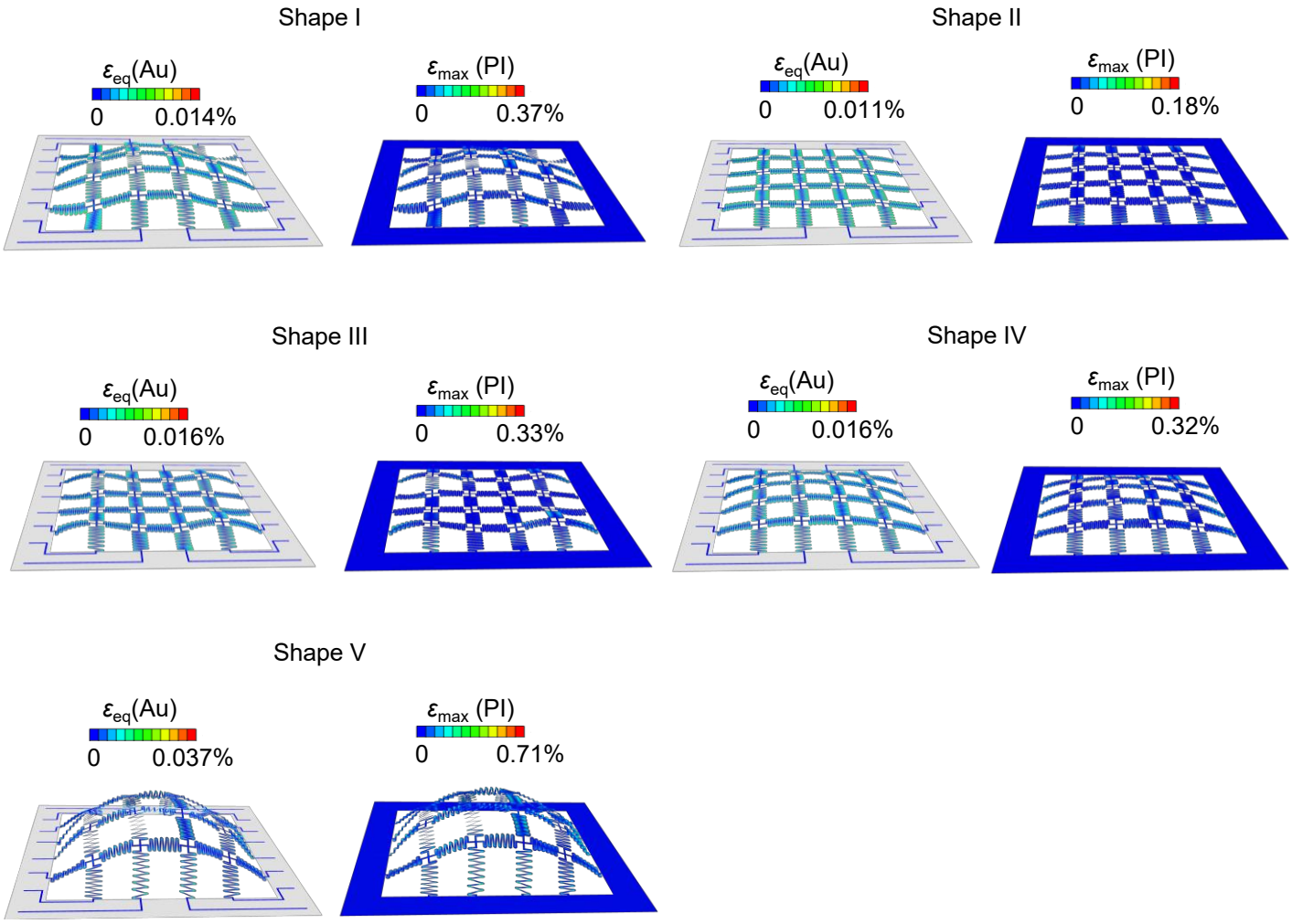

Supplementary Figure 18 | Distribution of the equivalent strain in Au and the maximum principal strain in PI for the 5 shapes of the falling droplet imitated by the 4x4 sample in Fig. 2b.

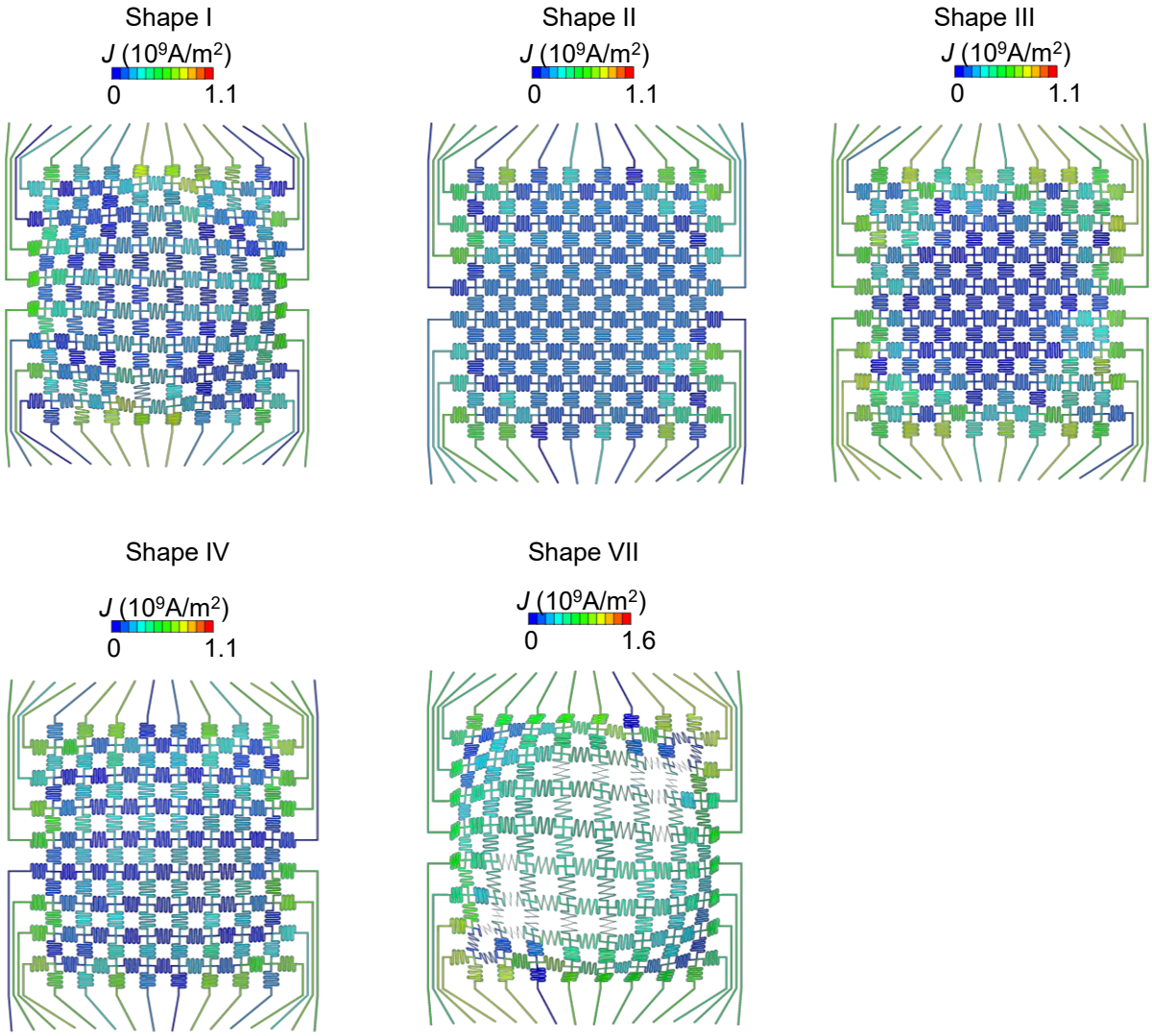

Supplementary Figure 19 | Distribution of current density for the 5 shapes of the falling droplet imitated by the 8×8 sample in Fig. 2c.

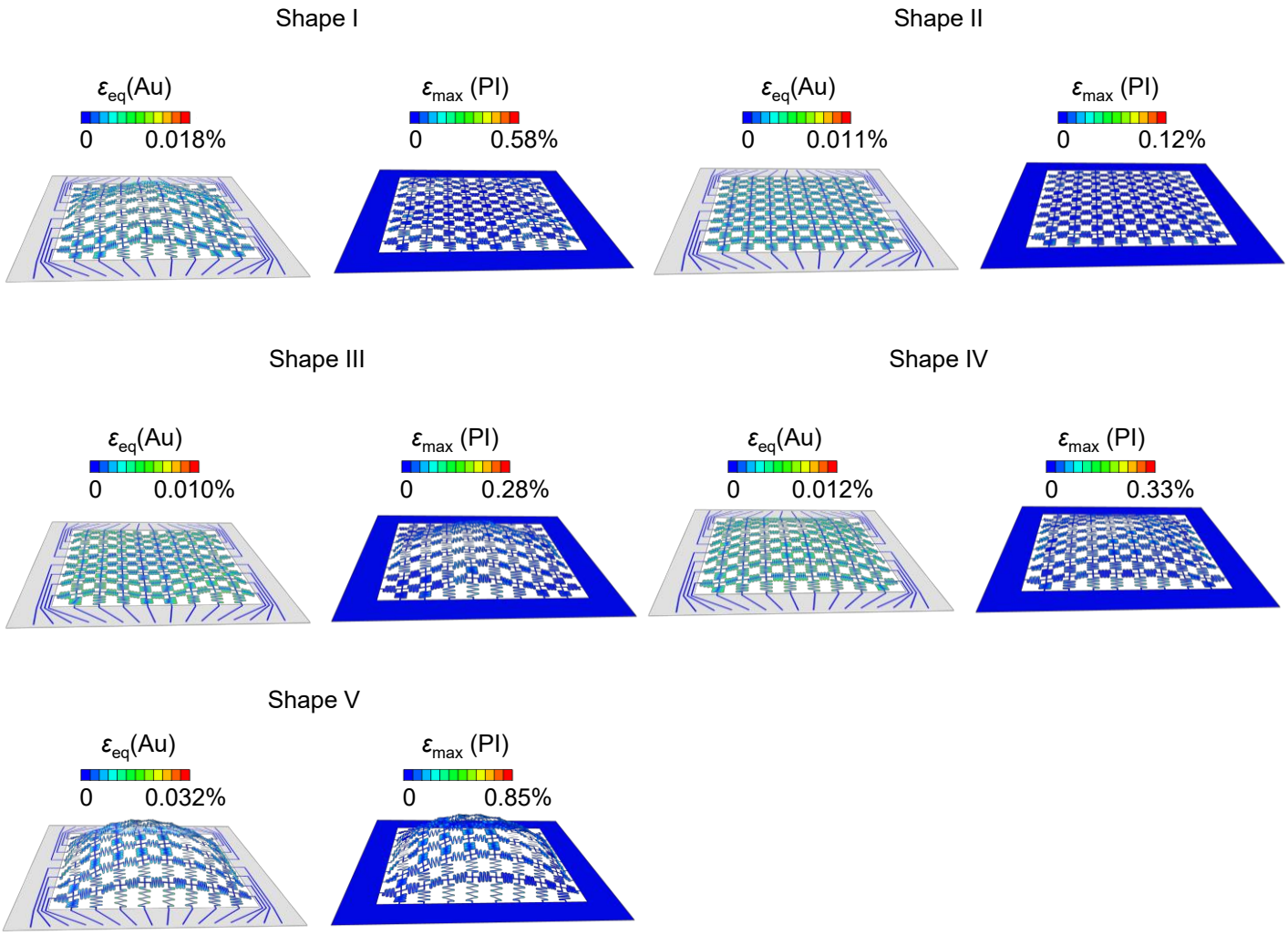

Supplementary Figure 20 | Distribution of the equivalent strain in Au and the maximum principal strain in PI for the 5 shapes of the falling droplet imitated by the 8×8 sample in Fig. 2c.

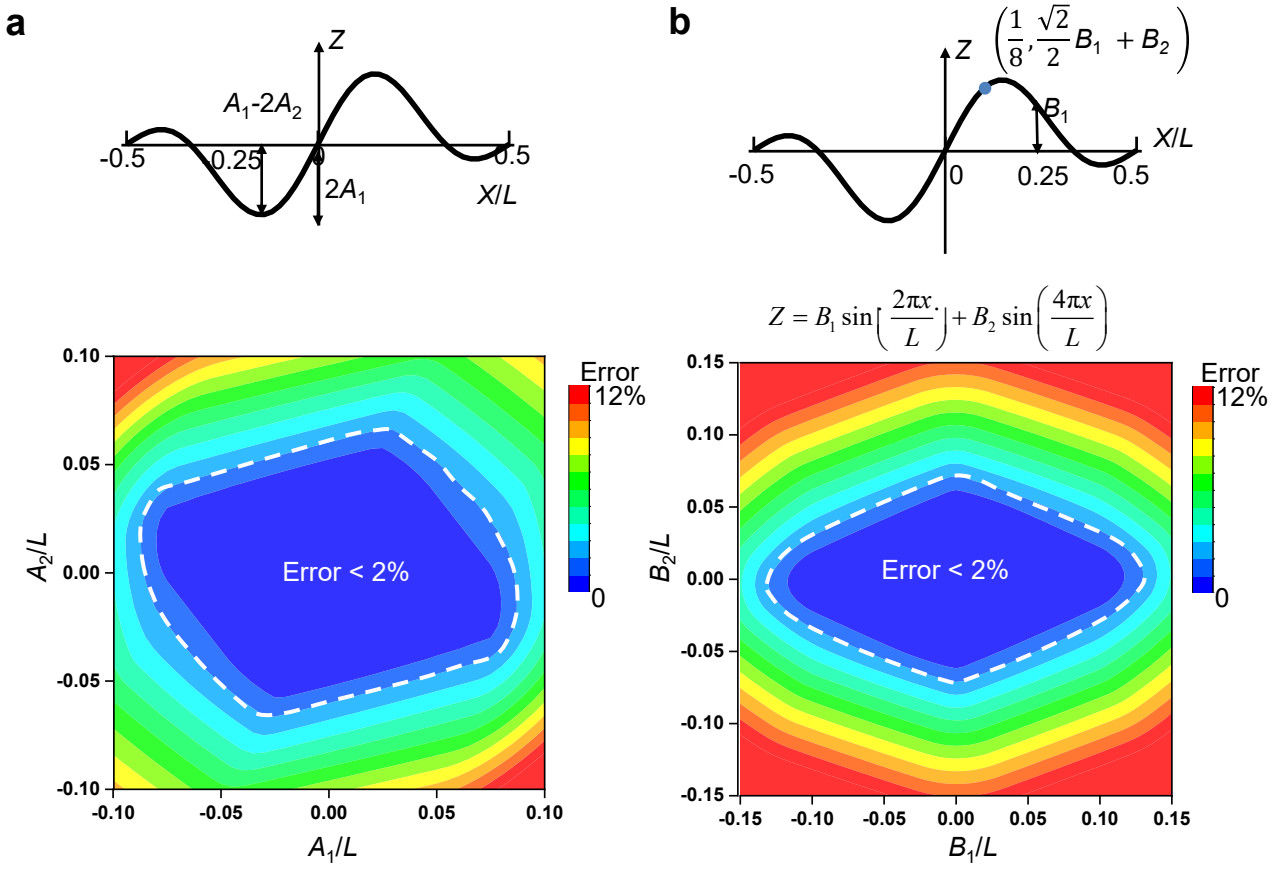

Supplementary Figure 21 | Error between the deformed an array of 8 serpentine beams and target shapes defined as the Fourier series with the first two terms. a, **b**, symmetric (a) and asymmetric (b) shapes with respect to the vertical axis at $X = 0$. With parameters in the region enclosed by the white dashed lines, the normalized error is smaller than 2%.

a

$$Z = A_1\left[\cos\left(\frac{2\pi X}{L}\right)+1\right]+A_2\left[\cos\left(\frac{4\pi X}{L}\right)-1\right]+A_3\left[\cos\left(\frac{6\pi X}{L}\right)+1\right]+A_4\left[\cos\left(\frac{8\pi X}{L}\right)-1\right]$$

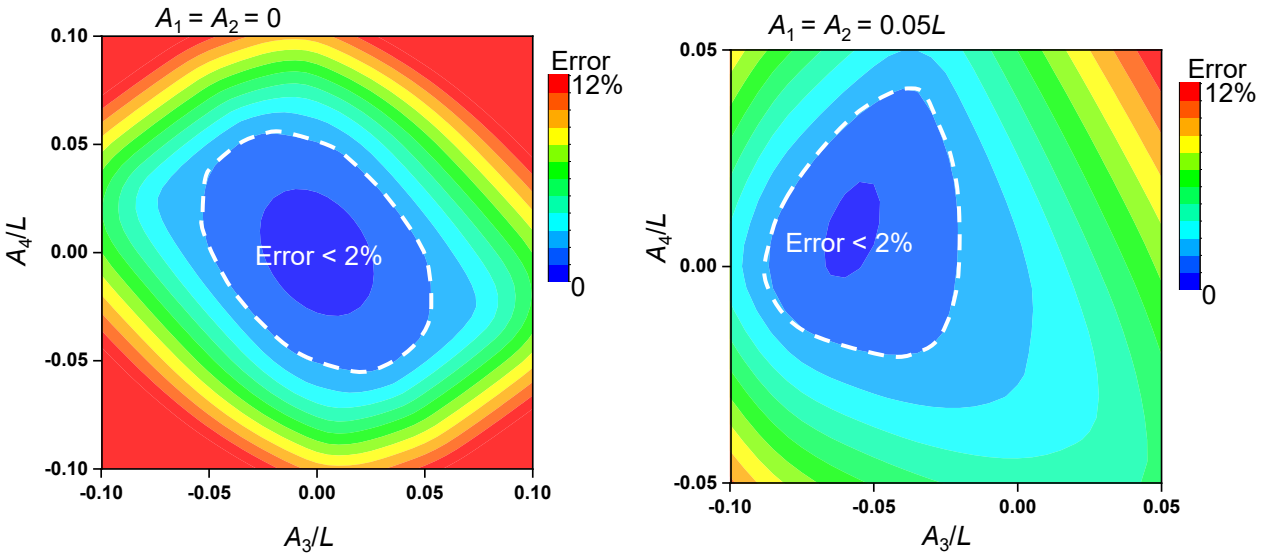

b

$$Z = B_1\sin\left(\frac{2\pi X}{L}\right)+B_2\sin\left(\frac{4\pi X}{L}\right)+B_3\sin\left(\frac{6\pi X}{L}\right)+B_4\sin\left(\frac{8\pi X}{L}\right)$$

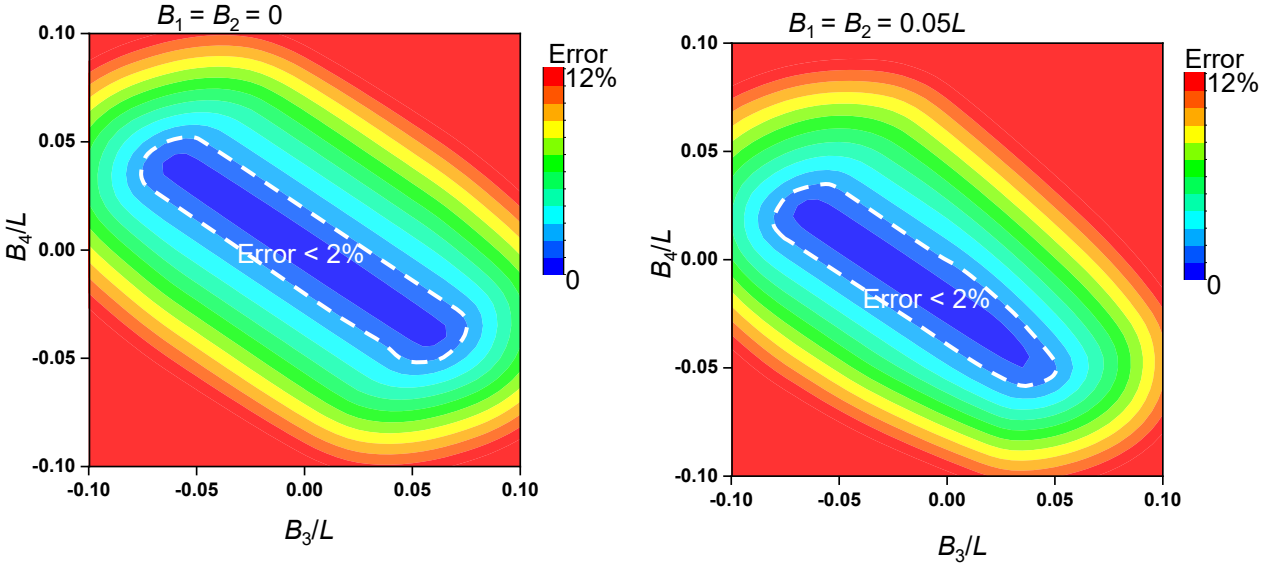

Supplementary Figure 22 | Error between the deformed an array of 16 serpentine beams and target shapes defined as the Fourier series with the first four terms. a, b, Symmetric. (a). and asymmetric (b) shapes with respect to the vertical axis at $X = 0$. With parameters in the region enclosed by the white dashed lines, the normalized error is smaller than 2%.

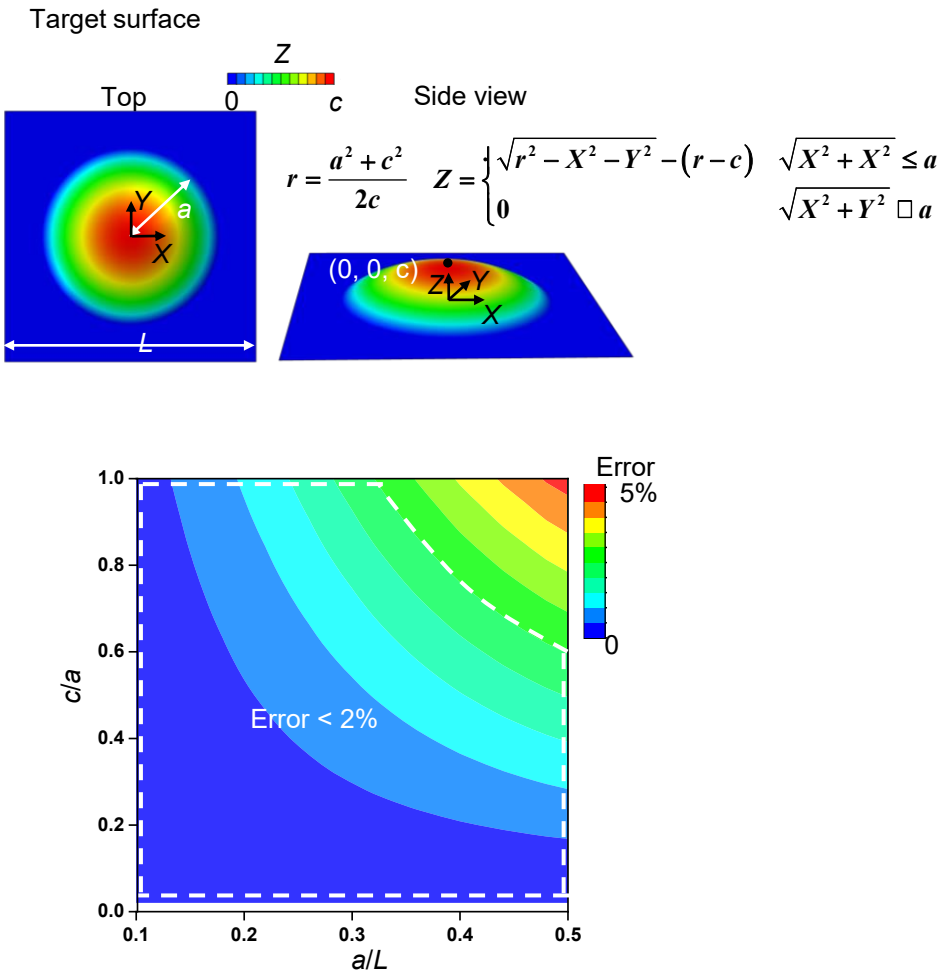

Supplementary Figure 23 | Error between the deformed 4×4 sample and target shapes defined by a spherical cap. With parameters in the region enclosed by the white dashed lines, the normalized error is smaller than 2%.

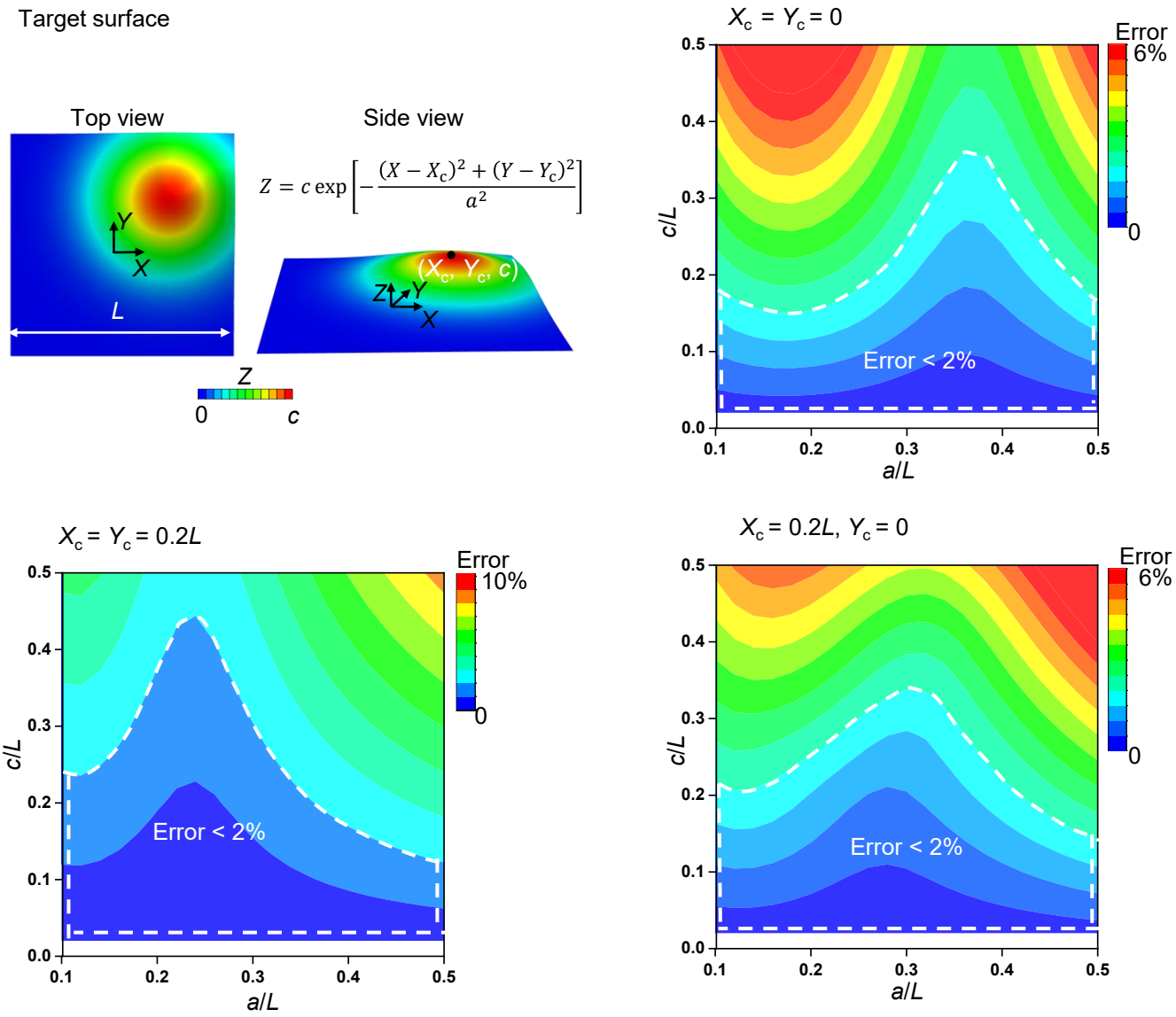

Supplementary Figure 24 | Error between the deformed 4×4 sample and target shapes defined by a Gaussian function. With parameters in the region enclosed by the white dashed lines, the normalized error is smaller than 2%.

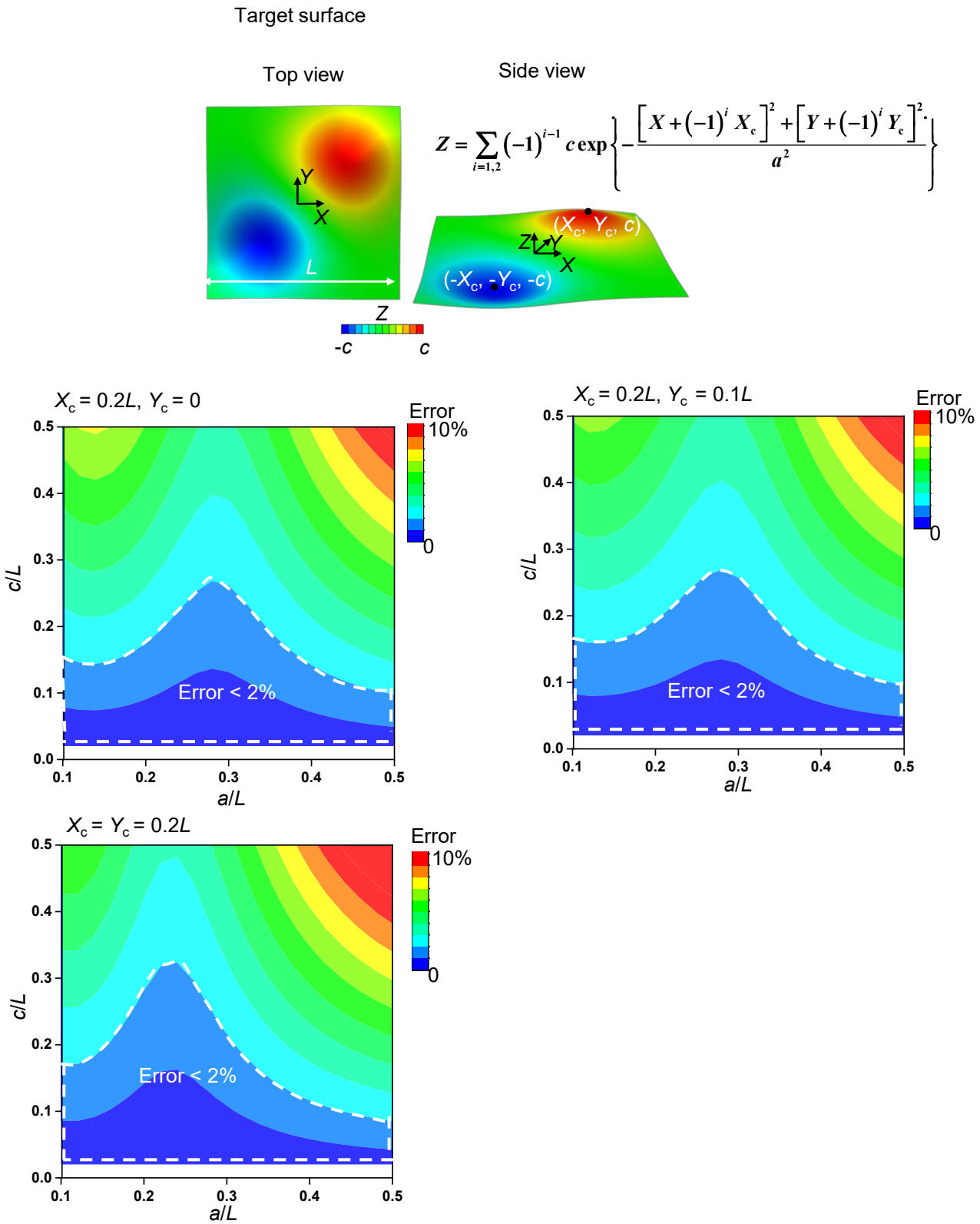

Supplementary Figure 25 | Error between the deformed 4×4 sample and target shapes defined by a Gaussian function with two terms. With parameters in the region enclosed by the white dashed lines, the normalized error is smaller than 2%.

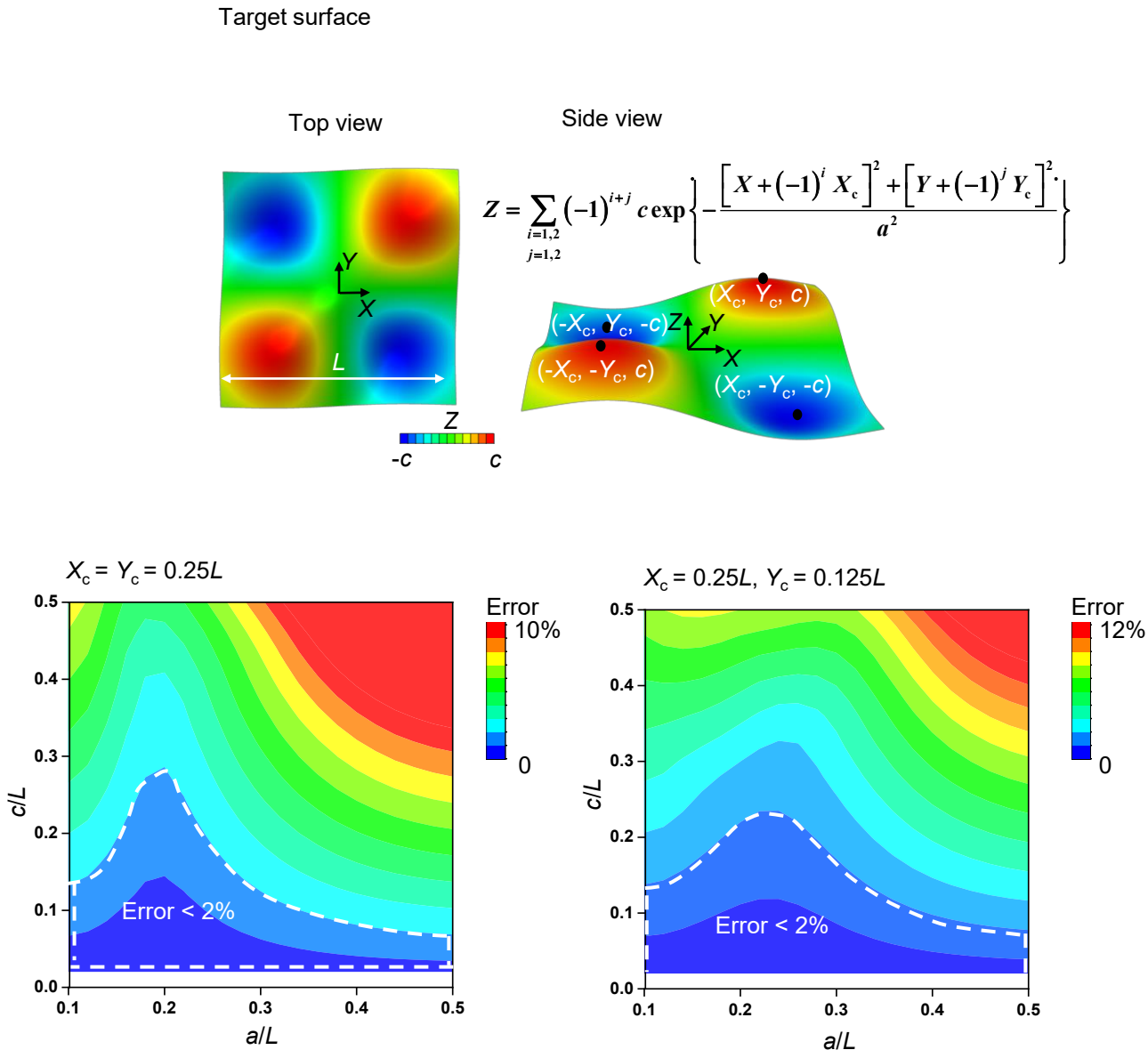

Supplementary Figure 26 | Error between the deformed 4×4 sample and target shapes defined by a Gaussian function with four terms. With parameters in the region enclosed by the white dashed lines, the normalized error is smaller than 2%.

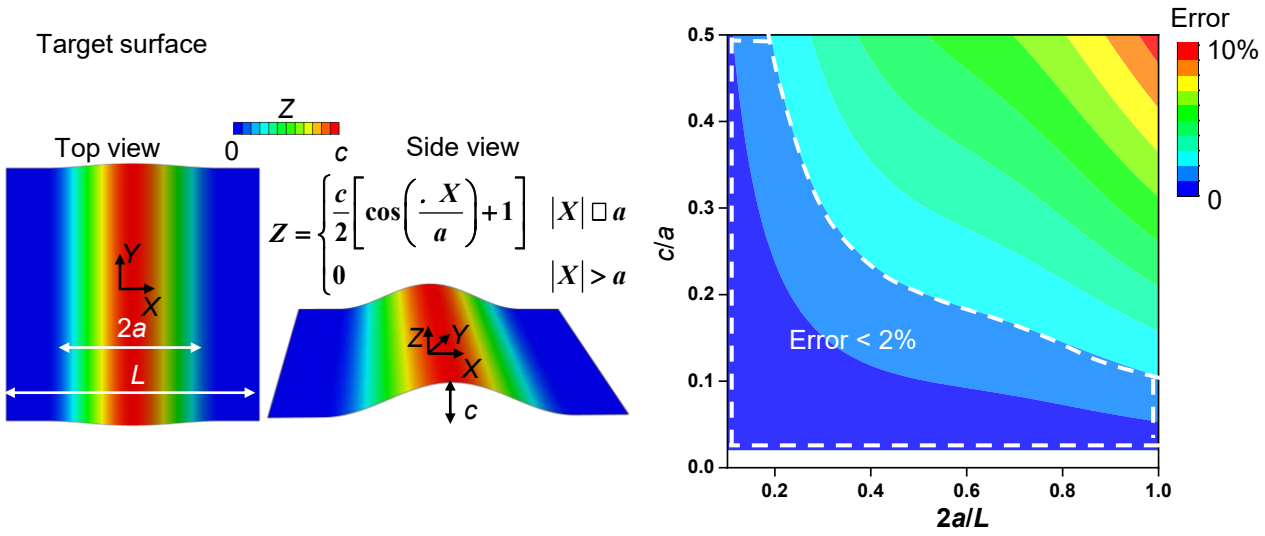

Supplementary Figure 27 | Error between the deformed 4×4 sample and target shapes defined by a sinusoidal function. With parameters in the region enclosed by the white dashed lines, the normalized error is smaller than 2%.

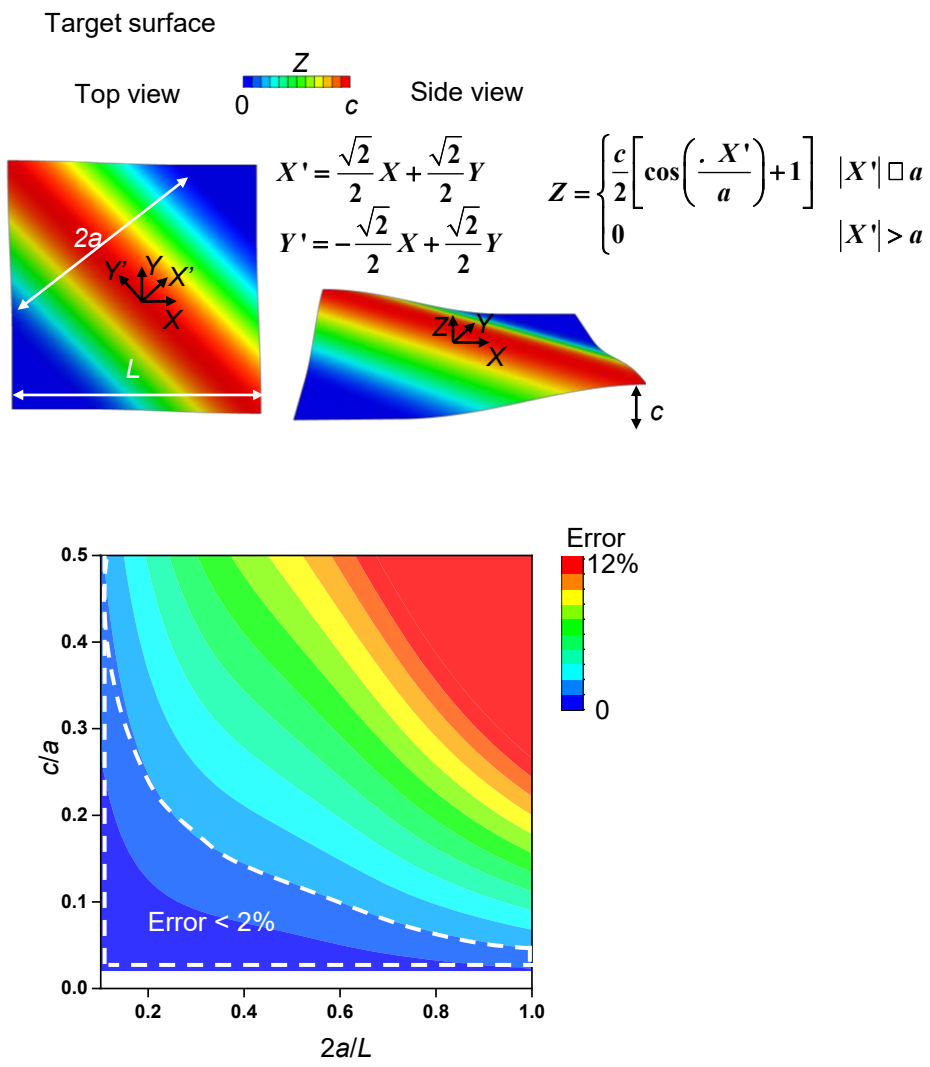

Supplementary Figure 28 | Error between the deformed 4×4 sample and target shapes defined by a sinusoidal function along the diagonal direction. With parameters in the region enclosed by the white dashed lines, the normalized error is smaller than 2%.

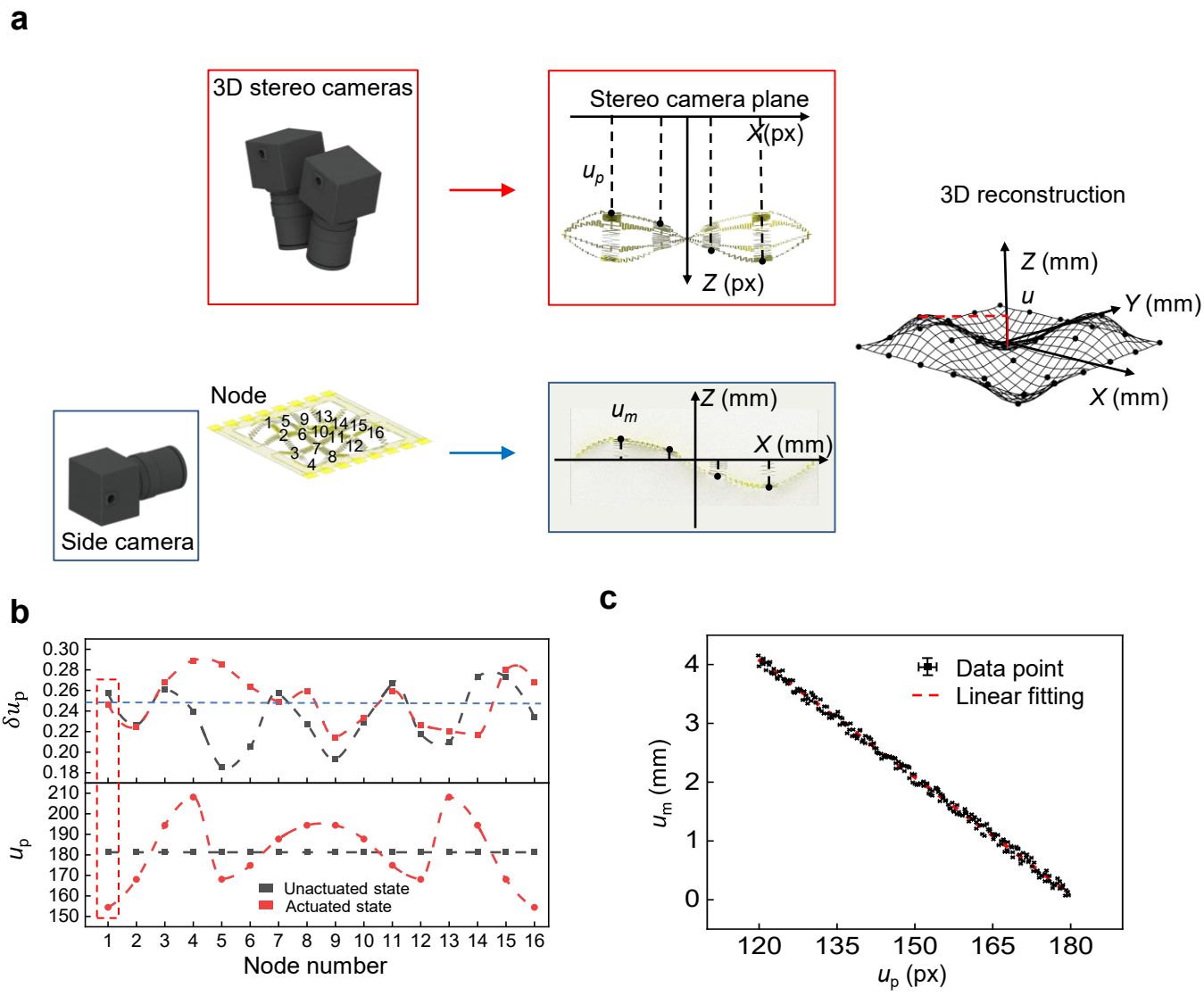

Supplementary Figure 29 | Characterization of the resolution and error of 3D imaging. **a,** The illustration of the 3D reconstruction characterization process. A side camera (Webcams, ELP, 3840 x 2160-pixel resolution, 30 fps) provides the measurement of nodal displacement (u_m) as the ground truth for 3D imaging calibration. Two cameras (Webcams, ELP, 3840x2160-pixel resolution, 30 fps) are placed symmetrically on the top of the sample. Stereo-imaging method reconstructs the real-time 3D shape of the sample, providing the depth measurement (u_p) between nodes and cameras in pixel units. The Deming regression models the relation between u_p and u_m that defines the 3D-reconstructed nodal displacement ($u(u_p)$). **c,** The depths (u_p) of the 16 nodes are measured by the stereo-imaging method when a 4×4 sample is under a cyclic actuation (200 cycles of shape IV in Supplementary Note S7). Both the actuated and unactuated distribution of measured depth (u_p) follow a Gaussian distribution. The result of analyzing the distribution of u_p of all 16 nodes reveals that the stereo-imaging method is capable of producing a measurement with a mean standard deviation of 0.25. **d,** The Deming regressor models the relation between u_p and u_m, providing the prediction for 3D-reconstructed displacement $u(u_p)$.

a

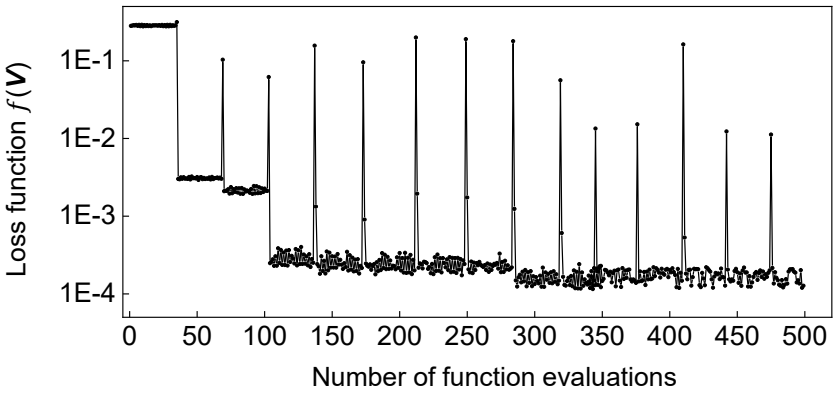

b

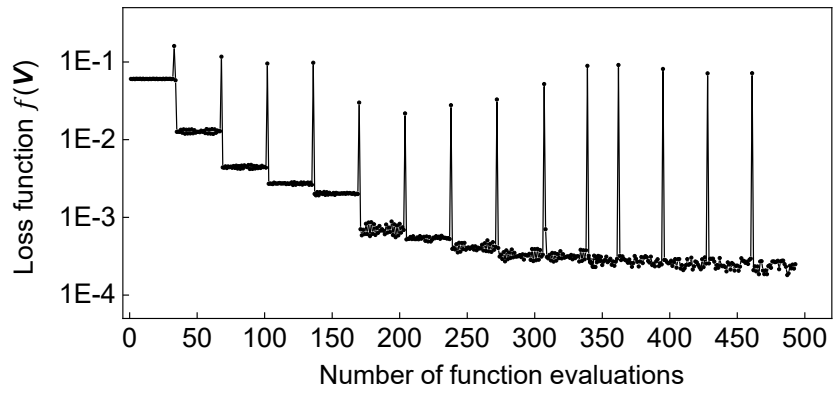

c

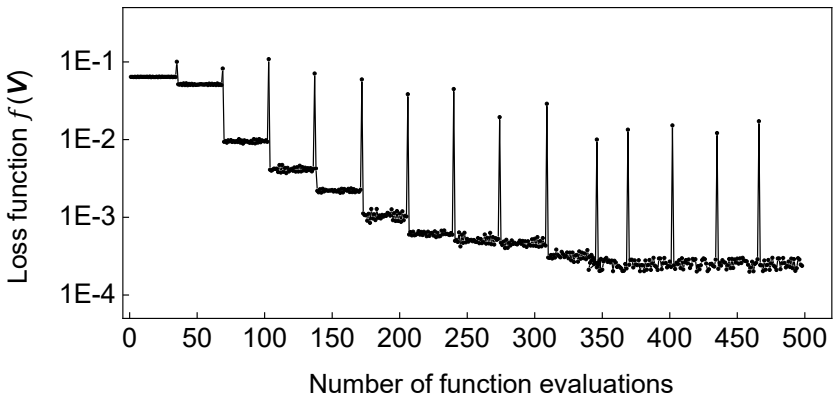

Supplementary Figure 30 | Typical descent of loss function over optimization iterations. a, b, c, For a 4×4 sample morphing into Shape I (a), III (b), IV (c), which are shown in Supplementary Note S7, the loss function $f(\boldsymbol{V})$(with an initial value $f(\boldsymbol{V}=0)$ in the range of 0.05-0.35) descends by ~99.5% to a steady state in 5-15 iterations. Each iteration takes 34 function evaluations given 32 input ports.

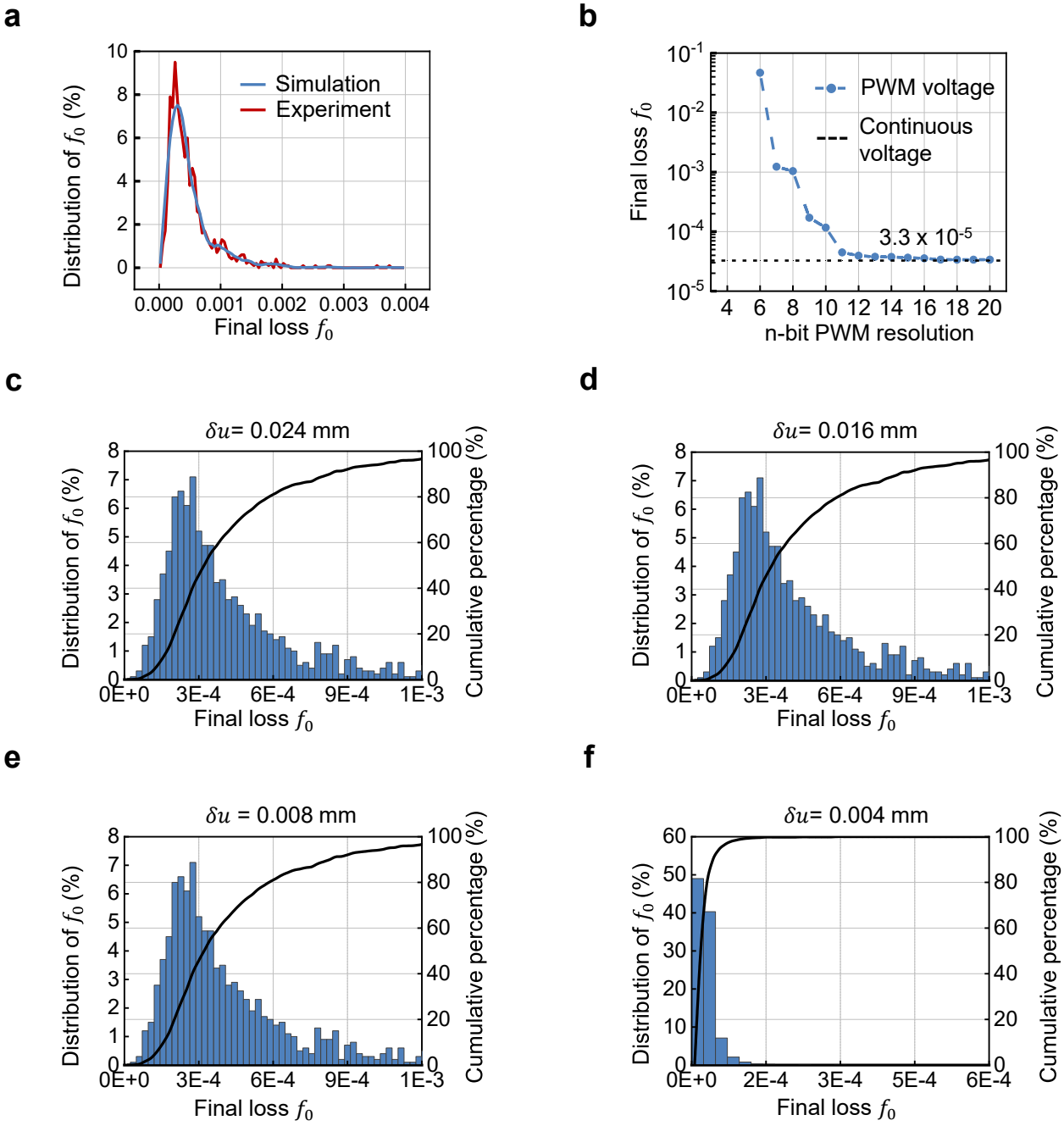

Supplementary Figure 31 | Simulation of the impact of experimental noises and constraints on the optimization process. a, The comparison between simulation (3D imaging noise δu = 0.016 mm, 12-bits PWM, maximum current I_{max} = 27 mA) and the experimental results of a 4×4 sample morphing into a target shape (Fig. 3b) from 1,000 trials. **b,** The simulation results of $f(\boldsymbol{V})$ with n-bit PWM voltage compared to the noise-free simulation with continuous voltage control. **c-f,** The distribution of the final loss f_0 after 15 iterations over 1,000 simulation trials morphing into the same target shape (Fig. 3b) with a decreasing 3D imaging uncertainty (δu) of 0.024 mm (c), 0.016 mm (d), 0.008 mm (e) and 0.004 mm (f).

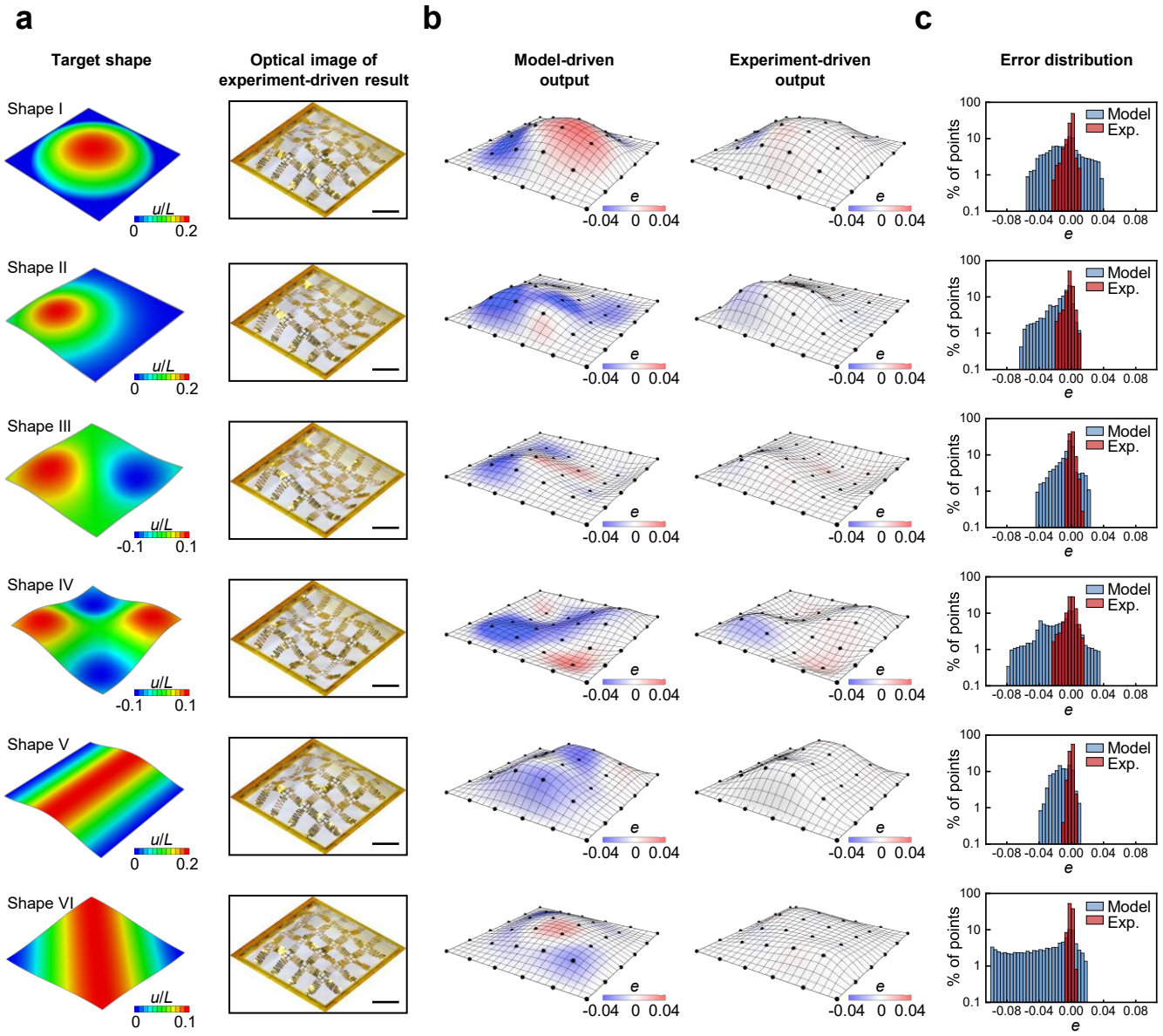

Supplementary Figure 32 | Experiment-driven self-evolving process in comparison with the model-driven approach. a, Target implicit shapes and optical images of the experiment-driven morphing results of a 4×4 sample. b, 3D reconstructed surfaces overlaid with contour plots of the minimized errors (e) and c, histograms of the minimized errors for model-driven and experiment-driven outputs. Scale bars, 5 mm.

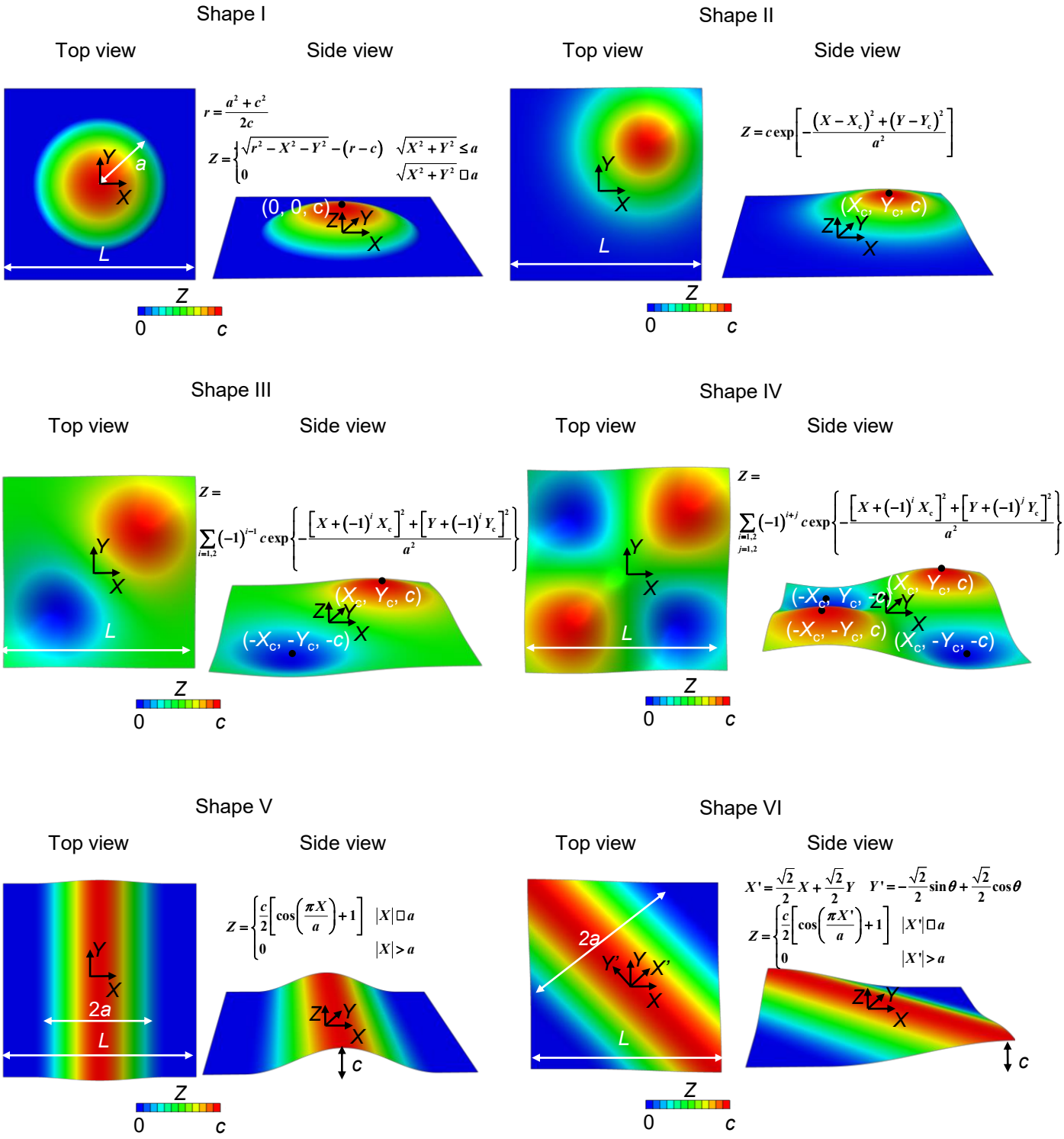

Supplementary Figure 33 | Schematic illustration and formula of 6 classes of implicit shapes.

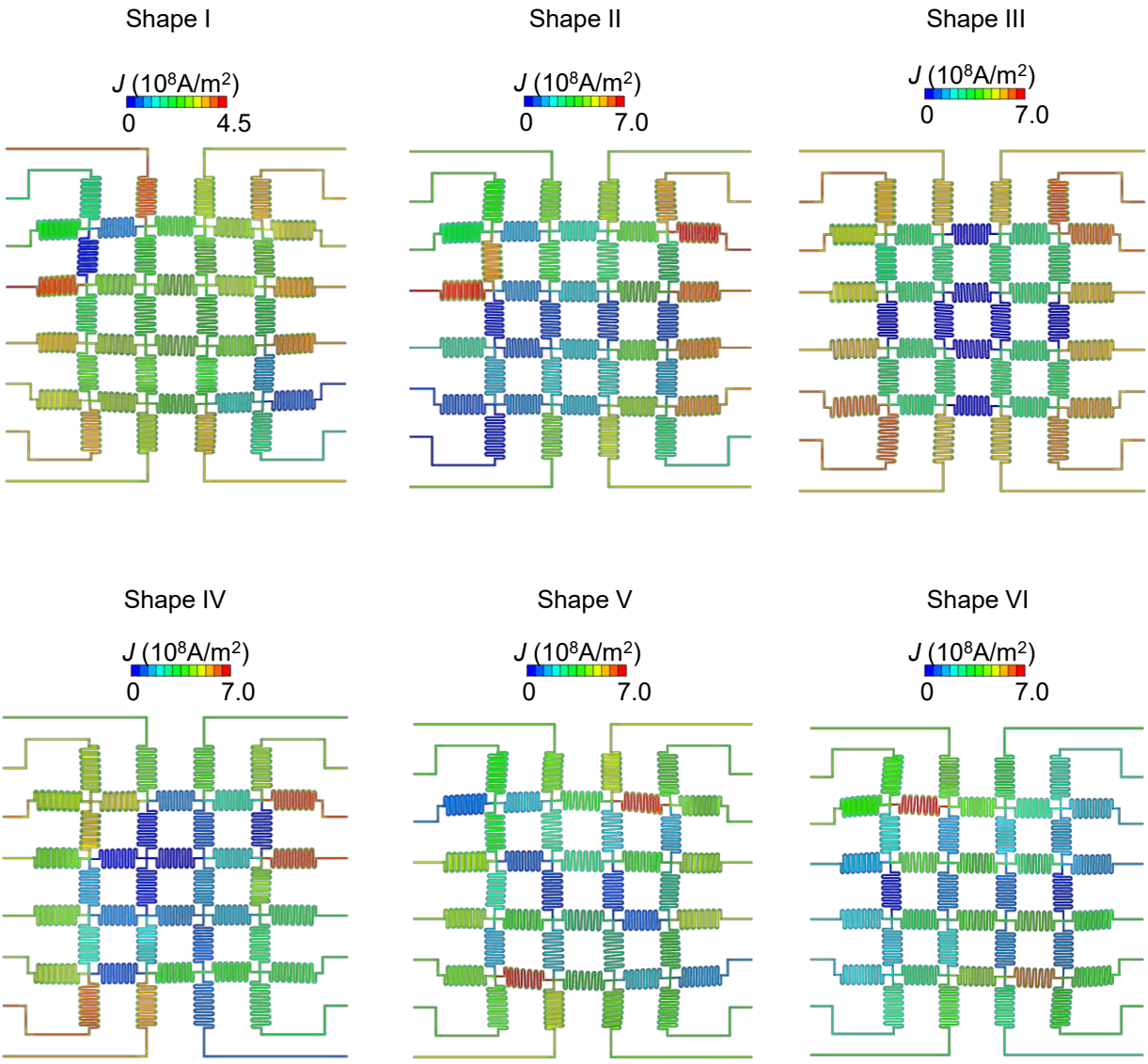

Supplementary Figure 34 | Distribution of current density for the 6 implicit shapes presented in Fig. 3b and Supplementary Fig. 32.

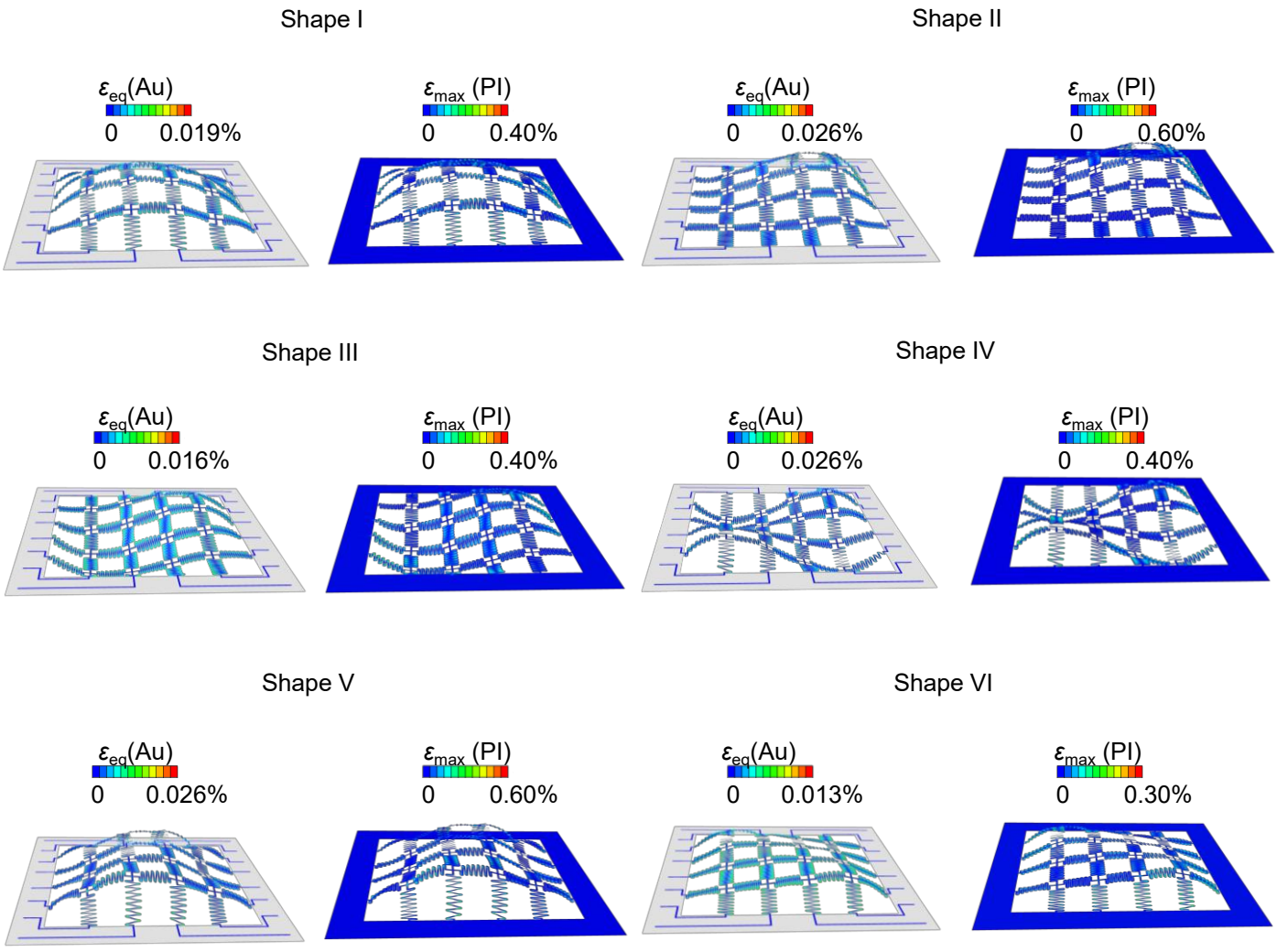

Supplementary Figure 35 | Distribution of the equivalent strain in Au and the maximum principal strain in PI for the 6 abstract implicit shapes presented in Fig. 3b and Supplementary Fig. 32.

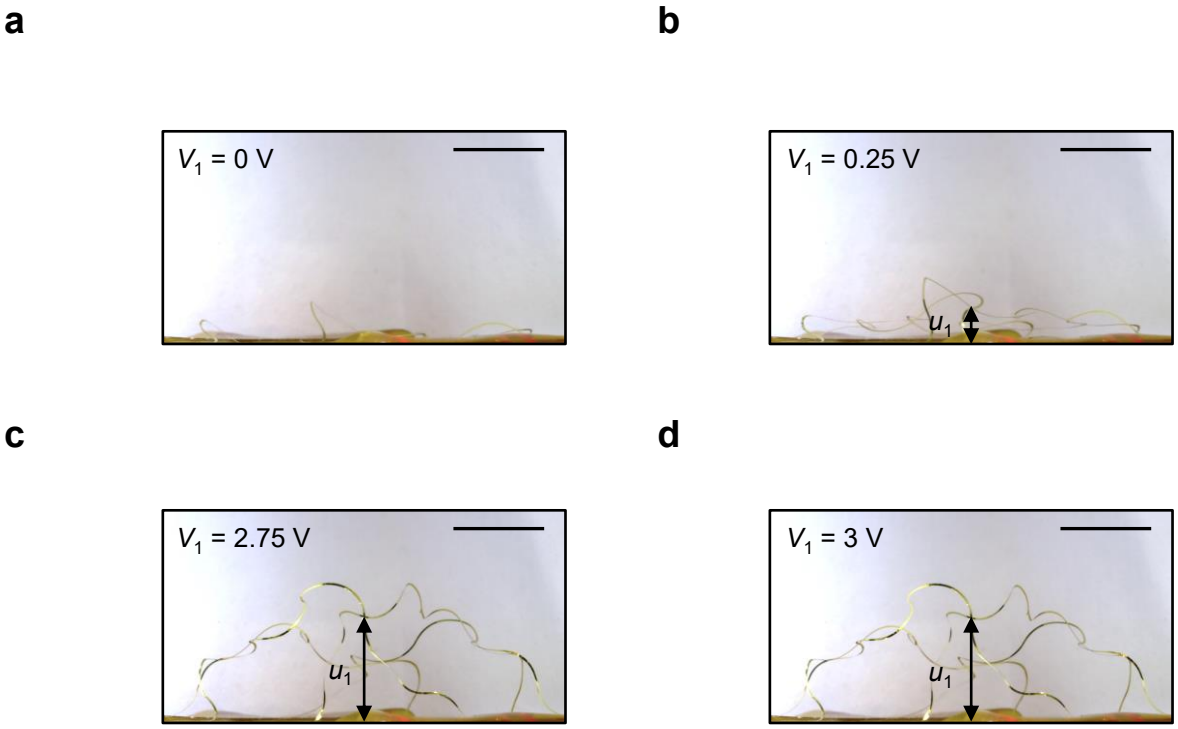

Supplementary Figure 36 | The optical images of a 2×2 sample with modified serpentine design for amplified nonlinear mechanical behavior in response to a range of actuation voltages. a, b, c, d, The side-view images of the sample deforming out-of-plane given an increasing voltage to port 1 (Fig. 4d) given V_1 = 0 V (a), 0.25 V (b), 2.75 V (c), and 3 V (d). The rate of change of u_1 decreases as the actuation voltage increases. Scale bar, 5 mm.

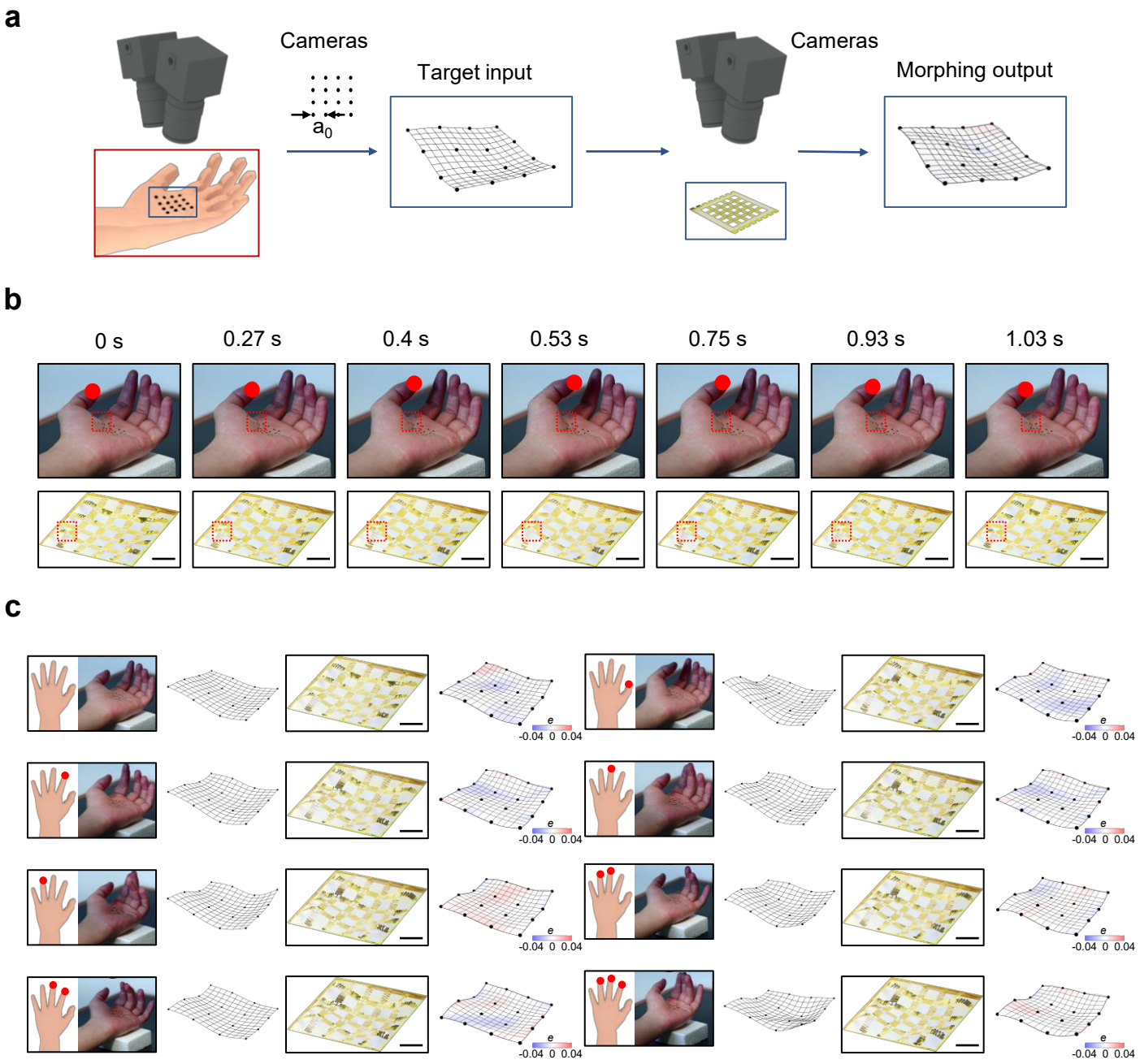

Supplementary Figure 37 | Self-evolving shape morphing toward semi-real-time shape learning. **a,** Schematic illustration of a duplicated stereo-imaging setup enabling a semi-real-time control of a 4×4 sample simulating the dynamic shape shifting of a palm surface with 4×4 markers. **b,** Experimental results of the continuous semi-real-time morphing of the palm surface with the thumb moving up. **c,** Morphing results of representative frames from a recording of hand making eight gestures related to different fingers moving. Scale bars, 5 mm.

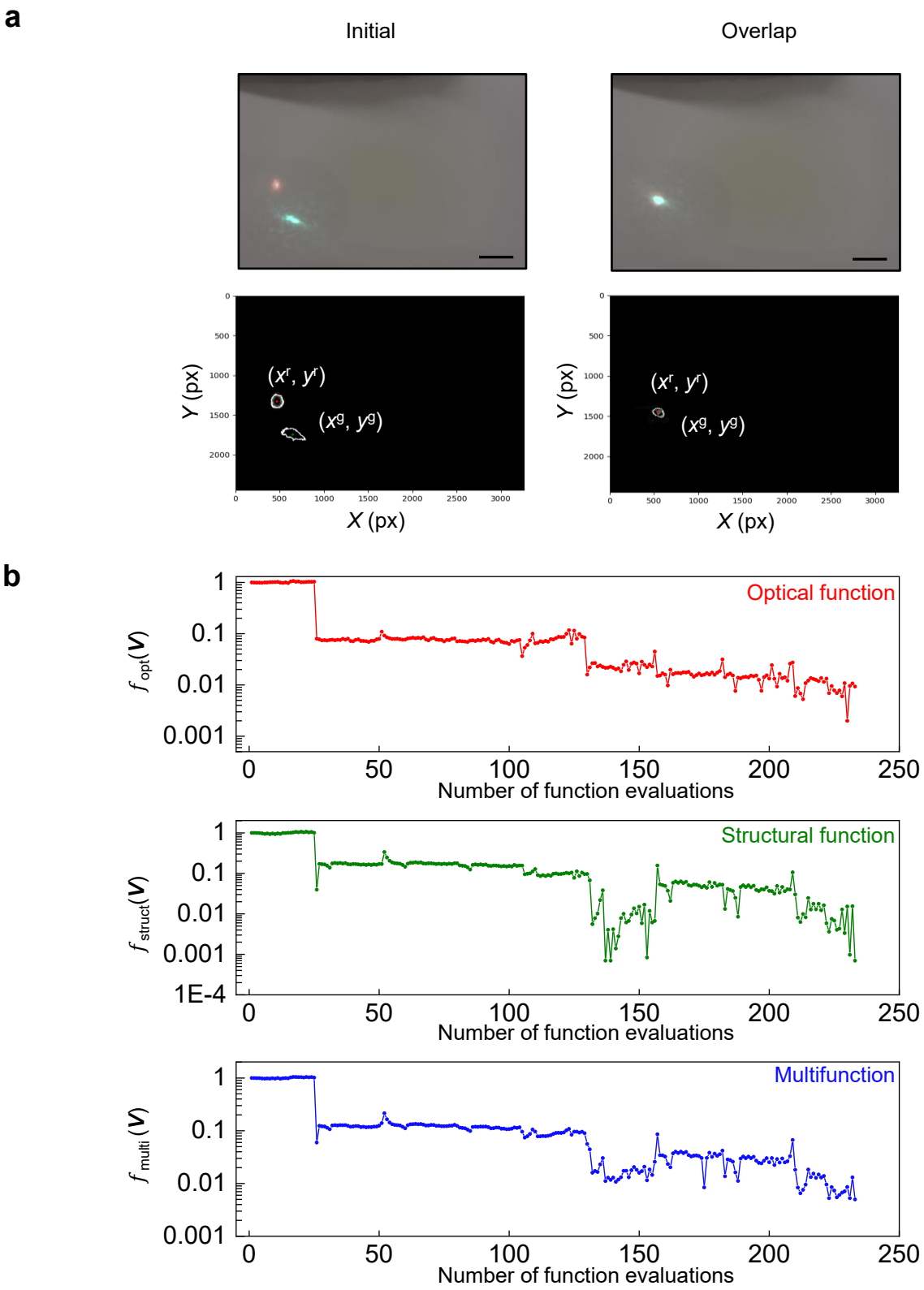

Supplementary Figure 38 | A 3×3 sample self-evolving to achieve an optical and a structural function simultaneously. a, Representative optical images of the laser spots on the receiving screen. The target optical function is to overlap two laser spots on the receiving screen. A customized imaging analysis method detects the centroid coordinates of the red/green laser spots as the current locations on the screen ($[x^{r/g}, y^{r/g}]$. **b,** A typical descent of loss functions over optimization iterations. The optimized loss function ($f_{\text{multi}}(\boldsymbol{V})$) is a linear combination of two parts: I) an optical loss function $f_{\text{opt}}(\boldsymbol{V})$ that evaluates the distance between the center of the two laser spots; II) a structural loss function $f_{\text{struct}}(\boldsymbol{V})$ that evaluates the central node displacement error. Scale bar, 5 mm.

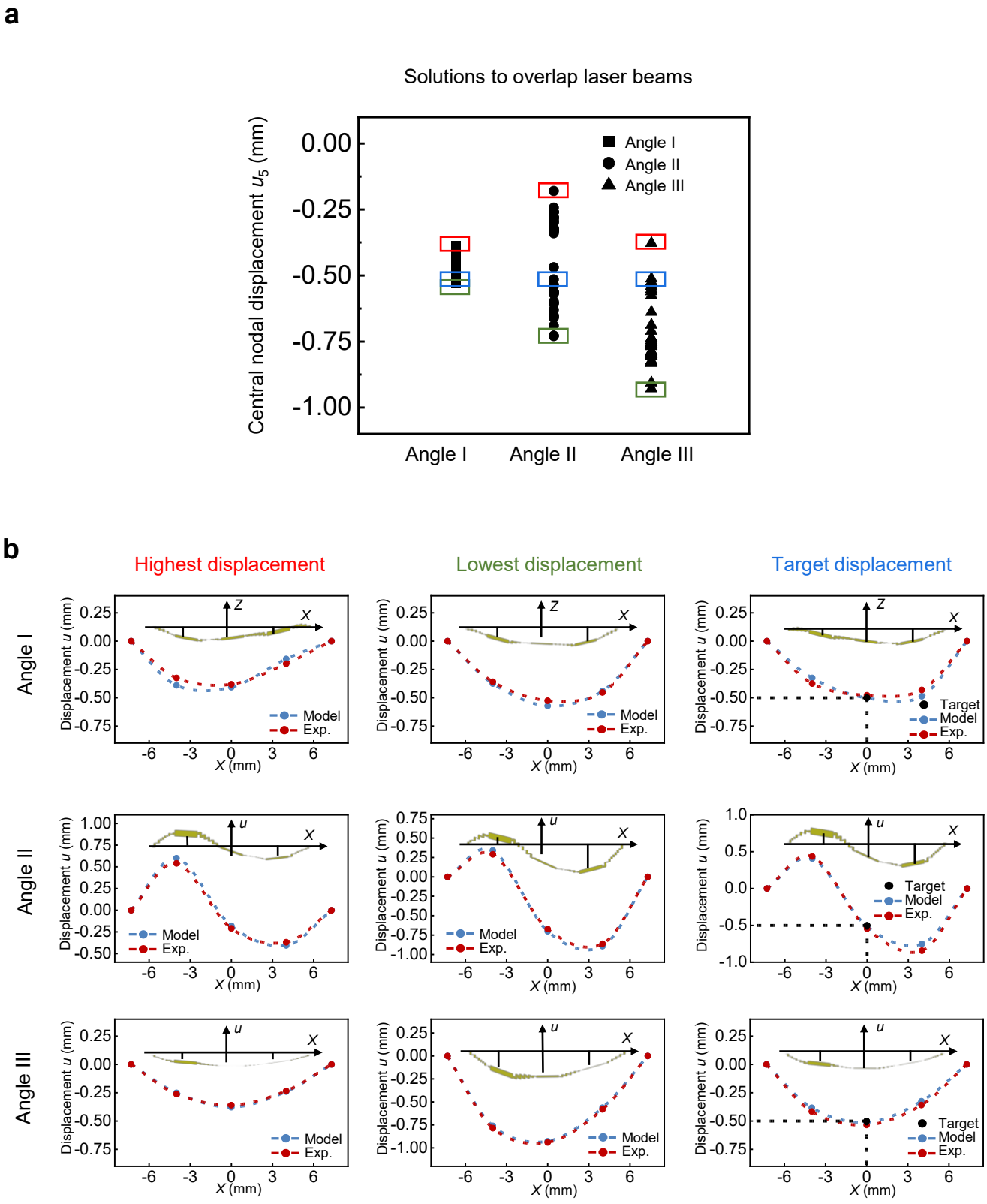

Supplementary Figure 39 | Allowed shape (structural-function) configurations of a 3×3 sample (Fig. 5c, d) when enforcing only the optical function. a, Allowed values of the central nodal displacement when enforcing only the optical function for three distinctive incident beam angles. **b,** Model predictions, and ex-situ 3D imaging results of the sample (side-view) overlapping the laser spots and in the configurations with the highest, lowest, and target central displacement.

Update Actuation	Wait for Steady State	3D imaging			Optimization	Sum
		Stereo Imaging	Template Matching	Projection and Reconstruction		
0.06 ± 0.01 s	0.1 ± 0.05 s	0.08 ± 0.04 s	0.11 ± 0.05 s	0.00 s	0.00 s	0.35 ± 0.15 s

Supplementary Table 1 | Function evaluation time profiling. An evaluation of the time budget of each step during the experiment-driven optimization of a 4×4 sample is presented. A function evaluation takes on average 0.35 s to complete.